6 Measuring optical backscattering in water

James M. Sullivan, Michael S. Twardowski, J. Ronald, V. Zaneveld, and Casey C. Moore

6.1 Introduction

Knowledge of light scattering can provide important information on underwater radiative transfer and the nature and dynamics of suspended particulate matter within a water mass. As an inherent optical property (IOP), scattering is represented by the volume scattering function (VSF), $\beta(\theta)$, which describes the angular dependence (θ) of scattered light from an incident unpolarized beam. It is defined as the radiant intensity $dI(\theta)$, scattered from a volume element dV, in a unit solid angle centered in direction θ, per unit irradiance E, i.e. $\beta(\theta) = (1/E)dI(\theta)/dV$. The scattering coefficienti, b, is determined by integrating the VSF from 0 to π radians (0° to 180°) according to:

$$b = 2\pi \int_0^{\pi} \sin(\theta)\beta(\theta)\, d\theta\,,$$

while the backscattering coefficient, b_b is determined by integrating the VSF in the backward direction (over $\pi/2$ to π radians, or 90° to 180°) according to:

$$b_b = 2\pi \int_{\pi/2}^{\pi} \sin(\theta)\beta(\theta)\, d\theta\,.$$

The angular shape and magnitude of oceanic VSFs are dependent on the water and associated dissolved salts, density fluctuations associated with turbulent mixing, and the resident particle assemblage (including bubbles). The VSF of pure water with salts is known spectrally and as a function of angle, temperature, and pressure within about 2% (Twardowski et al., 2007; Zhang and Hu, 2009). Turbulence effects, manifested as refractive index discontinuities, are constrained to the very near forward angles of the VSF (typically <0.1°) and are most significant in density gradients undergoing significant mixing (Bogucki et al., 1998; Agrawal, 2005; Mikklesen et al., 2008). Remaining shape and magnitude variability in the VSF is due to suspended particles.

The VSF of a particle assemblage is dependent on both the size and shape of the particles, as well as the refractive index of the component structural material(s) of each particle and their internal distribution (e.g. Bohren and Huffman, 1983; Quinby-Hunt et al., 1989; Zaneveld and Kitchen, 1995; Mishchenko et al., 2000).

A.A. Kokhanovsky, *Light Scattering Reviews 7: Radiative Transfer and Optical Properties of Atmosphere and Underlying Surface*, Springer Praxis Books, DOI 10.1007/978-3-642-21907-8_6,

An assemblage with larger particles will generally enhance forward scattering relative to backscattering (e.g., Morel, 1973; Stramski and Kiefer, 1991; Twardowski et al., 2001; Dall'Olmo et al., 2009). Since reflection processes are more dominant to backscattering, as opposed to the diffraction processes more dominant to forward scattering, particle composition (i.e. refractive index differences) will have a greater effect on backscattering (Mobley, 1994; Twardowski et al., 2001; Jonasz and Fournier, 2007).

Accurate quantification of the backscattered light field has applications to numerous disciplines of oceanography (Stramski et al., 2004), including studies of particle dynamics (abundances, size and composition), biogeochemical cycling, and both passive and active remote sensing (Ulloa et al., 1994; Twardowski et al., 2001; Boss et al., 2004a, b; Sullivan et al., 2005; Loisel et al., 2007; Stramski et al., 2008; Dall'Olmo et al., 2009; Twardowski et al., 2012). For example, remote sensing reflectance is approximately proportional to $b_b/(a + b_b)$ (Gordon et al., 1975), where a is the absorption coefficient. The shape and spectral dependence of the VSF in the backward direction forms a critical component of the Bidirectional Reflectance Distribution Function (BRDF), i.e., the variation of the upward radiance field with respect to the viewing and incident illumination angles (Morel and Gentili, 1983; Gordon, 1989; Morel et al., 1995; Zaneveld, 1995; Voss et al., 2000; Voss and Morel, 2005). With respect to biogeochemical cycling, algorithms linking backscattering and particle characteristics can be used as proxies for parameters such as chlorophyll, particulate organic carbon (POC), and total suspended matter (TSM) concentrations, as well as biological productivity (e.g. Behrenfeld and Falkowski, 1997; Stramski et al., 1999; Stramska and Stramski, 2005; Sullivan et al., 2005; Stramski et al., 2008; Twardowski et al., 2001, 2012; Sun et al., 2009, Neukermans et al., 2012). When used in conjunction with satellite remote sensing, these algorithms can extract information from surface oceans synoptically on a global scale. Active remote sensing systems, such as light detection and ranging (lidar) can typically penetrate deeper into the ocean than passive sensors and provide additional information on the vertical structure of backscattering, attenuation, and characteristics of associated particle fields. Interpretation of lidar signal returns are dependent on knowledge of backscattering in the very near backward direction, i.e. $\beta(\pi)$ (Guenther, 1985; Churnside et al., 1998; Churnside and Donaghay, 2009).

The backscattering ratio (b_b/b), or the proportion of light scattered in the backward direction, provides additional information on both water mass and particle characteristics. For example, using the slope of the particle size distribution (PSD) and the particulate backscattering ratio (b_{bp}/b_p), Twardowski et al. (2001) developed a model to estimate the bulk refractive index of particles. Backscattering measurements in conjunction with other IOP measurements have been used to discriminate particle types and dynamics in oceanic thin layer studies (e.g. Sullivan et al., 2005, 2010, Churnside and Donaghay, 2009), while the sinking flux of particle aggregates from the spring bloom in the North Atlantic was quantified using backscattering measurements from autonomous underwater vehicles (AUVs) (Briggs et al., 2011).

With VSF measurements made over suitable angular resolution and range, computing b or b_b can be a straightforward integration; however, there are currently (and historically), a very limited number of sensors capable of VSF measurements

over the required broad angular range (see review by Zhang et al., 2011). This is primarily due to the technical complexities of building such instruments, as well as a lack of focus perhaps on the VSF by the ocean optics community over the last several decades. Partly because of this complexity, interest evolved in the possibility of making a single VSF measurement weighted broadly as a function of angle in the backward direction to accurately estimate b_b (Oishi, 1990; Maffione and Dana, 1997; Boss and Pegau, 2001; Sullivan and Twardowski, 2009). These studies observed exceedingly low variability in the shape of backward scattering phase functions, lending credibility to using a single broadly weighted VSF measurement to approximate b_b. These findings proved critical to backscattering sensor designs that have emerged since the late 1990s. Such sensors can be constructed in a very small form factor, at low power and low cost. Several commercial designs have now been in regular use in a wide variety of applications and deployment modes (e.g. moorings, AUVs, vertical profilers) and have proved valuable in improving our understanding of particle dynamics in the ocean (Twardowski et al., 2005).

Herein, we review the principles of operation, evaluate calibration and measurement protocols, and measurement uncertainties for backscattering devices making one or more measurements of the VSF in the backward direction. This review also includes an assessment of the robustness of the relationships between the b_b and VSF measurements in the backward direction, and *in situ* comparisons of VSF estimates.

6.2 Generic sensor description

In their essential form, sensors measuring the VSF consist of a light source projecting into the water and a detector that collects light scattered into an acceptance aperture (Fig. 6.1). The detector (D) and the light source (S) are separated by a distance SD. The angle formed by the center of the detector field-of-view (FOV) and the line SD is θ_d. The half-angle of the detector FOV cone is σ_d. The corresponding angles for the source light beam are θ_s and σ_s. The nominal scattering angle of the sensor is $\gamma = \theta_s + \theta_d$. The intersecting volume formed from the source and detector conical beams is the sample volume.

The basic optical-electrical components of a VSF sensor include a source, such as a light emitting diode (LED) or laser, that couples to a detector, such as a photodiode or photomultiplier tube. A matched interference filter is usually employed to block out-of-band ambient light and re-emitted source radiation from inelastic sources such as Raman scatter and fluorescence. The spectral response of the sensor is determined by convolving the spectral band output of the source with the spectral characteristics of the detector assembly including the bandpass of the detector interference filter, and is normally modeled well as a Gaussian shape with associated centroid wavelength and full-width-half-maximum (FWHM) response. Using lenses and apertures, source and detector optical assemblies can be constructed to establish the desired VSF measurement geometry.

Calibration of VSF measurements requires the determination of instrument specific coefficients, termed scaling factors, which relate the device's detector response to $\beta(\theta)$. The specific angular response or weighting function of the measurement is

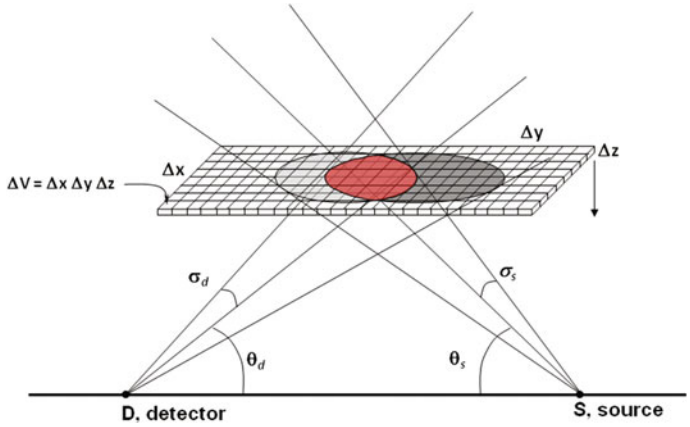

Fig. 6.1. Schematic drawing of backscattering sensor geometry. The intersection of the source and detector conical volumes and the $\Delta x \Delta y$ plane are ellipses, and the intersection of those ellipses (red shaded area) over Δz forms the effective sampling volume of the sensor.

dependent on the integrated relative signal response from each location within the sample volume. Three primary methods for calibrating VSF sensors are published in the literature. The first involves using a purified liquid standard such as benzene or toluene with a known VSF (Morel, 1966, 1974; Jackson et al., 1989). This is typically the preferred method of calibrating bench-top scattering devices, particularly those designed for quantifying colloids. The second, termed the 'plaque method' (Maffione and Dana, 1997; Dana and Maffione, 2002), measures the response of the instrument to a Lambertian target or plaque with a known reflectivity (e.g. Spectralon$^{\mathrm{TM}}$), as a function of distance, z, perpendicular to the $x - y$ plane of the sensor face containing source and detector (e.g. Fig. 6.1). The angular response function of the sensor is equivalent to this signal measured over its entire scattering volume, i.e. as a function of z. A complete mathematical derivation of this method is presented in Maffione and Dana (1997) and will not be reviewed here. The third approach relies on microspherical beads with known scattering characteristics and requires derivation of the sensor's angular weighting function through numerical analysis of its optical geometry (Moore et al., 2000; Twardowski et al., 2007, 2012). The details of this method are presented below.

6.3 Bead method calibration

6.3.1 Overview

The scattering meter measurement may be defined as (ignoring spectral dependencies):

$$\bar{\beta}(\bar{\theta}, \Delta\theta) = \int_0^{\pi} \beta(\theta) W(\theta)\, d\theta\,,$$

where $\bar{\theta}$ is the centroid angle computed as:

$$\bar{\theta} = \int_0^{\pi} \theta W(\theta)\, d\theta \Big/ \int_0^{\pi} W(\theta)\, d\theta\,,$$

and $\Delta\theta$ is the FWHM bandwidth of the weighting function, $W(\theta)$. The weighting function describes the probability distribution function for collected light for a given scattering measurement based on the optical geometry of the sensor.

The objective of calibrating the scattering sensor is to obtain a scaling factor, f, that can be used to convert raw signal measured by a detector into $\beta(\bar{\theta})$, the VSF evaluated at a centroid angle, $\bar{\theta}$, for a specific weighting function. To achieve this, $W(\theta)$ must be known, and raw scattering signal (proportional to power) must be measured in a solution of known VSF. A dark offset, D, must also typically be determined to remove any background electronic bias signal. Here, raw digital signal, typically in volts or digital counts, with D subtracted is represented as $N(\bar{\theta})$.

6.3.2 Determination of the weighting function, $W(\theta)$

The source light beam and FOV of the detector are both conical volumes that intersect to form the sample volume. One method of determining $W(\theta)$ is to numerically partition this sample volume into many small elementary volumes $\Delta V = \Delta x \Delta y \Delta z$, and then assess the contribution to $W(\theta)$ for each ΔV (refer to Fig. 6.1). The simplest way to do this is to numerically step a Δz-plane parallel to the sensor face through the sample volume, assessing the contribution of the many ΔV's that occur at the intersecting source and detector ellipses for each step. This method relies on a precise knowledge of the source and detector beam geometries. Note that the drawing in Fig. 6.1 shows the source and detector beams originating as points rather than discrete area cross-sections, as is the case in most practical implementations of the sensor. In the numerical analysis, beams emerging from the sensor face can be traced back to points (S and D, respectively) and an imaginary SD line is drawn, representing the 'effective' sensor face and z-plane (refer to Figs. 6.1 and 6.2). Note that for some geometries with large scattering angles and very wide beam spreads, the sampling volume may not be discrete and theoretically can be infinite. Letting Z be the distance from the SD line to the intersection of the middle of the source and detector beams, contributions to the returned signal (and the weighting function) become negligible at a z-plane of about $15Z$ because of the $1/r^2$ effect in irradiance propagation for the source beam and scattered light. In the numerical analysis, a Z_{max} must be set and this can be varied accordingly to assess where the contributions from farther z-planes become negligible.

The first step in computing $W(\theta)$ is determining if a specific $\Delta V = \Delta x \Delta y \Delta z$ above the sensor face is in the sample volume. With z in the same plane as the sensor face and SD line, from simple geometry we see that:

$$r_s(x, y, z) = \sqrt{x^2 + y^2 + z^2}\,,$$
$$r_d(x, y, z) = \sqrt{x^2 + (SD - y)^2 + z^2}\,,$$

and

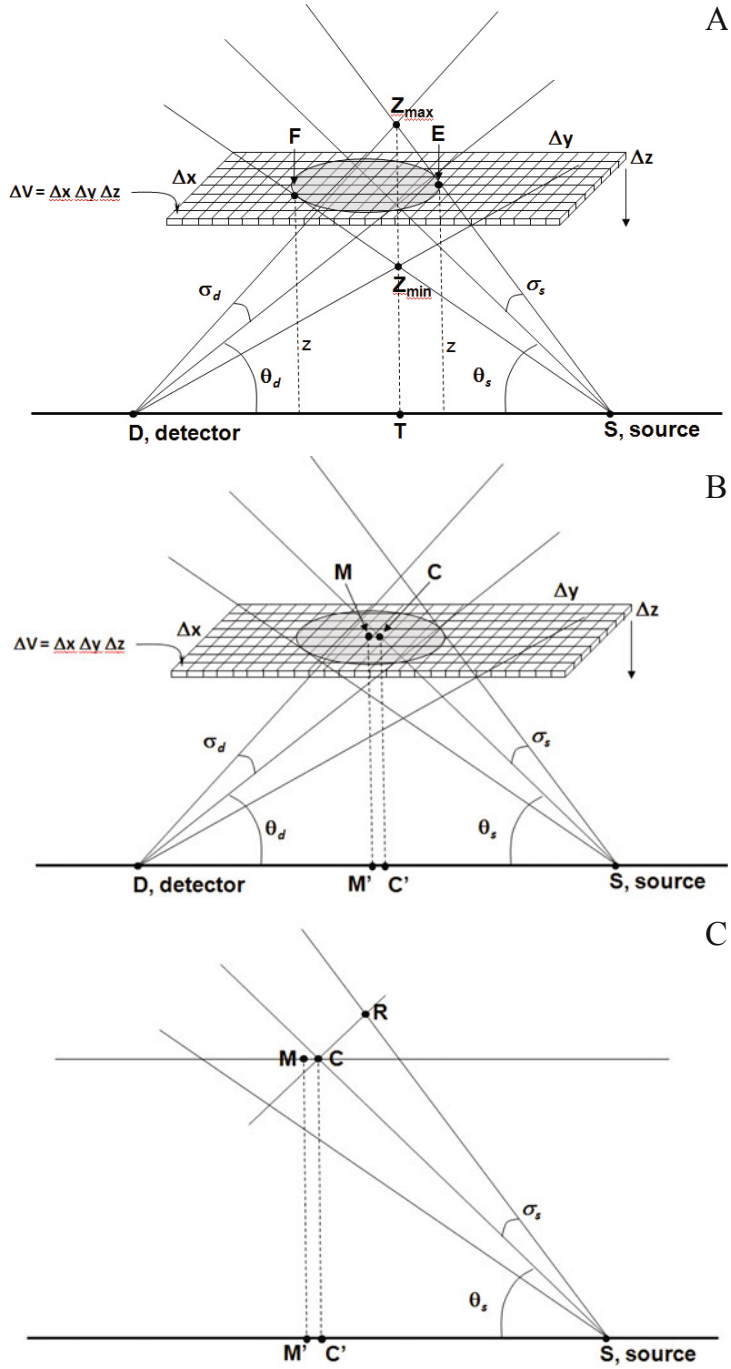

Fig. 6.2. Schematic drawings for derivation of sensor geometries

$$\cos(\pi - \gamma) = \frac{r_d^2 + r_s^2 - SD^2}{2 r_d\, r_s}$$

where r_s and r_d are the distances from the source (S) to ΔV and the detector (D) to ΔV, respectively, and γ is the scattering angle formed between the light beam from S to ΔV and from ΔV to D. Additionally,

$$\tan \alpha_s = \frac{z}{\sqrt{x^2 + y^2}}\,,$$

and

$$\tan \alpha_d = \frac{z}{\sqrt{(SD - y)^2 + x^2}}\,.$$

The solid angle of the source beam is,

$$\Omega_s = \pi(\tan \sigma_s)^2\,,$$

and similarly for the detector FOV,

$$\Omega_d = \pi(\tan \sigma_d)^2\,.$$

The intersection of the source beam cone and a plane defined by z is an ellipse (if the illuminated area of the plane is finite). If the semi-major and semi-minor axes of the ellipse are given by a_{majs} and a_{mins}, respectively, where the additional 's' subscript indicates the source parameters, the equation of the source beam ellipse at level z is derived as follows (refer to Figs. 6.2(A) and 6.2(B)):

$$SF = z \cot(\theta_s - \sigma_s)\,,$$

$$SE = z \cot(\theta_s + \sigma_s)\,,$$

and

$$2a_{majs} = z\big[\cot(\theta_s - \sigma_s) - \cot(\theta_s + \sigma_s)\big]\,.$$

The minor axis does not occur at the center of the cone, C, but rather at the middle of the ellipse, M. The projection of C on the SD plane is C' and the projection of M is M'. Hence,

$$C'S = z \cot \theta_s\,,$$

and

$$SM' = SE + a_{majs}\,.$$

Thus,

$$C'M' = CM = SM' - C'S = SE + a_{majs} - z \cot \theta_s\,.$$

From a side view of the source beam, we can see that (refer to Fig. 6.2(C)):

$$\frac{CR}{CS} = \tan \sigma_s\,,$$

$$CR = CS \tan \sigma_s\,,$$

and

$$CS = \frac{z}{\sin\theta_s}\,,$$

$$CR = \frac{z\,\tan\sigma_s}{\sin\theta_s}\,.$$

The equation of our ellipse is:

$$\frac{x^2}{a_{mins}^2} + \frac{y^2}{a_{majs}^2} = 1\,,$$

with $(x,\, y) = 0$ at M.

The chosen coordinate system sets $z = 0$ at the SD plane, $y = 0$ at the plane passing through S orthogonally to the SD line, and $x = 0$ at the plane passing through the SD line orthogonally to the SD plane (i.e., z-plane).

We already know a_{majs}. We need to determine a_{mins} for $x = CR$, and $y = -MC$ at the ellipse. Substituting these into the ellipse equation yields:

$$a_{mins}^2 = \frac{CR^2}{1 - [CM/a_{majs}]^2}.$$

The center of the ellipse is at $x = 0$, $y = SM'$. The equation of the ellipse is thus:

$$\frac{x^2}{a_{mins}^2} + \frac{(y - SM')^2}{a_{majs}^2} = 1\,.$$

All relevant parameters have been derived. Any volume ΔV at (x, y, z) is illuminated by the source if the value of (x, y) in the left-hand side of the equation returns a value $\leq$1.

Derivation of the detector FOV ellipse is similar, where the terms G and H are analogous to the terms E and F, respectively, in the source derivation above. We will use the 'd' subscript to indicate detector FOV parameters:

$$2a_{majd} = z[\cot(\theta_d - \sigma_d) - \cot(\theta_d + \sigma_d)]\,,$$

$$DG = z\cot(\theta_d + \sigma_d)\,,$$

$$DH = z\cot(\theta_d - \sigma_d)\,,$$

$$DM' = DG + a_{majd}\,,$$

$$CR = \frac{z\tan\sigma_d}{\cos\theta_d}\,,$$

$$CM = DM' - z\cot\theta_d\,,$$

and

$$a_{mind}^2 = \frac{CR^2}{1 - [CM/a_{majd}]^2}\,.$$

The equation of the detector ellipse at level z is:

$$\frac{x^2}{a_{mind}^2} + \frac{[y - (SD - DM')]^2}{{a_{majd}}^2} = 1\,.$$

All points (x, y, z) are within the detector FOV if their value returns ≤ 1 for the left-hand side of the equation.

It is of use in the programming to determine the limits of the illuminated and detected volumes (refer to Fig. 6.2):

$$\frac{Z_{max}}{DT} = \tan(\theta_d + \sigma_d)\,,$$

and

$$\frac{Z_{min}}{TS} = \tan(\theta_s - \sigma_s)\,.$$

DT plus TS are equal to SD, which is known. Thus,

$$Z_{min} = SD/\left[\frac{1}{\tan(\theta_d - \sigma_d)} + \frac{1}{\tan(\theta_s - \sigma_s)}\right],$$

and

$$Z_{max} = SD/\left[\frac{1}{\tan(\theta_d + \sigma_d)} + \frac{1}{\tan(\theta_s + \sigma_s)}\right].$$

The source maximum, Y_{maxs}, is equal to $SF = SE + 2a_{majs}$; the source minimum, Y_{mins}, is equal to SE; the detector maximum, Y_{maxd}, is equal to $SG = SD - DG = SH + 2a_{majd}$; the detector minimum, Y_{mind}, is equal to $SH = SD - DG - 2a_{majd}$. The maximum of x (X_{max}) is the smaller of a_{mind} or a_{mins}. The volume of interest (effective sampling volume) is thus defined by,

$$\left\{\begin{array}{l} x : 0 \text{ to } X_{max} \text{ (multiply by 2 to get the complete volume)} \\ y : \text{the larger of } Y_{mins} \text{ and } Y_{mind} \text{ to the smaller of } Y_{maxs} \text{ and } Y_{maxd} \\ z : Z_{min} \text{ to } Z_{max}\,. \end{array}\right\}$$

To obtain the weighting function, $W(\theta)$, the returned power is determined for each elementary volume found to reside in the sample volume, and integrated over the illuminated area (detector footprint) so that the power detected, P_d, is related to the source beam power, P_s, according to:

$$P_d(x, y, z) = P_s \beta\big(\gamma(x, y, z)\big) W(x, y, z)\,,$$

Powers P_d and P_s need to be solved at each ΔV to solve for $W(x, y, z)$. The solid angle for P_s is defined as,

$$\Omega_s = \pi \tan^2 \sigma_s\,.$$

The irradiance at $\Delta V$is determined as follows: an area $\Delta A = \Delta x \Delta y$ at an angle, $(90 - \alpha_s)$, to the center of the source beam has a solid angle of:

$$\Omega(\Delta V) = \frac{\Delta x \Delta y \cos(90 - \alpha_s\,(x, y, z))}{r_s^2(x, y, z)}\,.$$

The power received by $\Delta V(x, y, z)$ is

$$P(\Delta V) = P_s \frac{\Omega(\Delta V)}{\Omega_s} .$$

This power of the beam traveling from the source to (x, y, z) is attenuated by

$$e^{-cr_s(x,y,z)} .$$

Thus, the irradiance, or power per unit area, at (x, y, z) is

$$E(x, y, z) = \frac{P(\Delta V)}{\Delta x \Delta y} = \frac{P_s \cos(90 - \alpha_s(x, y, z))}{r_s^2(x, y, z)\Omega_s} \, e^{-cr_s(x,y,z)} .$$

The scattering angle between the light ray from the source to $\Delta V(x, y, z)$ and the light ray from ΔV to the detector is defined by $\gamma(x, y, z)$.

Since, by definition,

$$\beta(\gamma) = \frac{dI(\gamma)}{E\, dV} ,$$

by rearrangement,

$$dI(\gamma) = \beta(\gamma)\, E\, dV .$$

Hence,

$$dI\big(\gamma(x, y, z)\big) = \beta\big(\gamma(x, y, z)\big)\, E(x, y, z)\Delta x \Delta y \Delta z, \;\; \text{(units of place Watts sr}^{-1}) ,$$

and

$$dI = P/\Omega_d(x, y, z) .$$

The power received at the detector due to scattering at ΔV is then:

$$P_d(x, y, z) = dI\big(\gamma(x, y, z)\big)\Omega_d(x, y, z)\, e^{-cr_d(x,y,z)} .$$

Ω_d is the detector solid angle for ΔV:

$$\Omega_d\,(x, y, z) = \frac{\Delta x \Delta y \cos\big(90 - \alpha_d(x, y, z)\big)}{r_d^2(x, y, z)} .$$

Substituting, we obtain:

$$\begin{aligned} P_d(x, y, z) =& \beta\big(\gamma(x, y, z)\big)\, E(x, y, z)\, \Delta x \Delta y \Delta z \\ & \times \frac{\Delta x \Delta y \cos\big(90 - \alpha_d(x, y, z)\big)}{r_d^2(x, y, z)} \, e^{-cr_d(x,y,z)} , \end{aligned}$$

The weighting function $W(x, y, z)$ can now be solved, setting P_s at unity for simplicity:

$$W(x, y, z) = E(x, y, z)\Delta x \Delta y \Delta z\, \Omega_d \, e^{-cr_d}$$

where $W(x, y, z)$ is the weighting function for $\Delta V(x, y, z)$ with the associated scattering angle γ. The sum of all $W(x, y, z)$ for angles γ yields the total weighting

function and is normalized to the total sum of all weights (so that the value of P_s is irrelevant):

$$\sum_x \sum_y \sum_z W(x, y, z) = 1 .$$

Weighting functions can be determined as described for each unique source–detector pair dependent on instrument design.

The above assumes that the incident power, P_s, is equivalent throughout its beam cross-section. With many sources such as LEDs and lasers, the source image approximates a Gaussian intensity distribution. Such an intensity distribution can be applied as an additional weighting in the numerical analysis.

6.3.3 Determining theoretical phase functions

With the weighting function known, a hydrosol with a known $\beta(\theta)$ must be used to calibrate the sensor. This hydrosol can be created in the laboratory with a solution of purified water and polystyrene microspherical beads with National Institute of Standards and Technology (NIST) traceable size distributions and known complex refractive index. Using the bead manufacturer's reported value for the real part of the refractive index and Ma et al., (2003) for the imaginary part is recommended. Microspheres have been used in calibrating many different scattering devices (e.g., Volten et al., 1998; Lee and Lewis, 2003; Sullivan and Twardowski, 2009; Twardowski et al., 2011). Particle size distribution functions for the beads are modeled according to a Gaussian shape using the mean size and standard deviations reported from the bead manufacturer. Particulate phase functions, $\tilde{\beta}(\theta) = [\beta_p(\theta)/b_p]$, for these bead particles can be determined with Lorenz–Mie theory (Bohren and Huffman, 1983). Phase functions should be computed for at least 300 evenly spaced particle sizes spanning ±3 standard deviations from the mean to ensure an accuracy better than 1%. The phase function for each particle size is then weighted according to the size distribution function, and summed to give the phase function for the entire population. By convolving the computed phase function with the sensor weighting functions (section 6.3.2), the appropriately weighted phase function, $\tilde{\beta}(\bar{\theta}_i, \Delta\theta_i)$ can be determined. The effect of spectral response associated with each unique source and detector can be additionally considered by imposing a spectral weighting in the phase function computation, although for sufficiently narrow spectral weightings (10–20 nm FWHM), associated errors are typically <2% (Twardowski et al., 2007).

6.3.4 Experimental calibration and application

For the laboratory part of the calibrations, a clean sensor is mounted in a covered test tank filled with 0.2 μm filtered fresh water from a polishing water purification system with resin cartridges to remove organic substances. The inside walls of the tank should have a minimally reflective surface (flat black) and the tank should accommodate an open cylindrical volume in front of the sensor face large enough to ensure any reflections from the tank wall will not contaminate the signal. Measurements with the sensor can then be taken over a concentration series of serially added microspherical beads. Beads should be sonicated prior to use with

no shaking before addition to the tank, as recommended by the manufacturer. In addition to the volume scattering measurements, the total scattering coefficienti b can be measured concurrently using a beam attenuation meter. Polystyrene bead absorption is negligible in comparison to bead scattering, so that the c measurement can represent b with an accuracy better than 1%. The $\beta(\theta)$ may then be obtained for any concentration of beads by multiplying the theoretical phase function by measured b, with the provision that the b component of the theoretical phase function is computed using an acceptance angle matching the attenuation measurement. In practice, to maximize accuracy, experimental data should be collected at several bead concentrations and used to obtain a least-squares linear slope between b and the raw signal N from the VSF measurement. Since we are only concerned with the response of the sensors to the bead additions (i.e., the slope), no background subtractions are necessary, i.e., the observed responses are only a function of added beads. The slope can be considered an experimental phase function, $\tilde{\beta}_e(\bar{\theta}_i)$, in terms of counts m^{-1} or $\mathrm{V\,m}^{-1}$. Calibration scaling factors, $f(\bar{\theta}_i)$ in units of $\mathrm{m}^{-1}\,\mathrm{sr}^{-1}$ counts^{-1} or $\mathrm{m}^{-1}\,\mathrm{sr}^{-1}\,\mathrm{V}^{-1}$ are then obtained by dividing the theoretically derived phase function, $\tilde{\beta}(\bar{\theta}_i)$, (see section 6.3.3) by the experimental phase function, $\tilde{\beta}_e(\bar{\theta}_i)$. At this point, basic calibration of the sensor is complete. Note that the concentration of beads does not need to be known with this calibration method.

To process field measurements or lab measurements of unknown solutions, raw signal from the sensor is converted to $\beta(\bar{\theta}_i)$ $(\mathrm{m}^{-1}\,\mathrm{sr}^{-1})$, by first subtracting the background dark offset, D, and then multiplying the resulting value by the calibration scaling factor, $f(\bar{\theta}_i)$. Note that corrected measurements of $\beta(\bar{\theta}_i)$ include the VSF of pure water and any associated dissolved salts. The full relationship between the raw signal (after dark offset subtraction) and $\beta(\bar{\theta}_i)$ is:

$$N(\bar{\theta}_i)\, f(\bar{\theta}_i) = N(\bar{\theta}_i)\, \tilde{\beta}(\bar{\theta}_i)/\tilde{\beta}_e(\bar{\theta}_i) = N(\bar{\theta}_i)\, \tilde{\beta}(\bar{\theta}_i) \,/\, [N(\bar{\theta}_i) \,/\, b] = b\, \tilde{\beta}(\bar{\theta}_i) = \beta(\bar{\theta}_i)\,.$$

6.3.5 Dependence of the scattering signal on attenuation

There is attenuation of a sensor's incident and scattered beams over its pathlength, i.e. the distance from the light source to the sample volume to the detector. Attenuation losses result in scattering measurements being underestimates of the true scattering of the solution. Expanding on the formula above to include the attenuation effect (Twardowski et al., 2012):

$$\beta(\bar{\theta}_i) = N(\bar{\theta}_i) f(\bar{\theta}_i)\, e^{L[b_p \varepsilon + a_{pg} + a_w]}\,,$$

where $N(\bar{\theta}_i)$ is the raw signal after dark offset subtraction, $f(\bar{\theta}_i)$ is the scaling factor with units $\mathrm{m}^{-1}\,\mathrm{sr}^{-1}\,\mathrm{counts}^{-1}$ or $\mathrm{m}^{-1}\,\mathrm{sr}^{-1}\,\mathrm{V}^{-1}$, L is the total pathlength from source window to sample volume to detector window, b_p is the particulate scattering coefficient, ε is the fraction of scattering by particles along the optical path (other than the primary scattering event in the sample volume) that is not ultimately measured by the detector, a_{pg} is the absorption by particulate and dissolved material, and a_w is the absorption by pure water with any dissolved salts. Each elementary scattering volume has a specific pathlength, which can be numerically determined from geometry in the weighting function calculations (see section 6.3.3). Integrating

over all elementary volumes in the sample volume gives the total dependence on attenuation and an effective pathlength, L_e, for the attenuation effect. The error due to attenuation along the path is minimized when the effective pathlength L_e is as small as possible. The attenuation dependence can be viewed as two separate components: light lost due to scattering and light lost due to absorption. The pure water contribution is constant and the a_{pg} contribution can be measured independently if necessary. The scattering contribution is minimized when ε is as small as possible. The scattering fraction ε can be represented as

$$\frac{\int_0^\pi W_\varepsilon(\theta)\beta(\theta)\,d\theta}{\int_0^\pi \beta(\theta)\,d\theta},$$

where W_ε is the angular weighting function for ε. To minimize ε, W_ε should be small, particularly at the near-forward angles where $\beta(\theta)$ is strongly peaked in natural waters. This can be achieved through sensor geometry by using widely dispersed source and detector beams to provide a relatively large sample volume target for light scattered along the path from the source, and a large footprint detector to provide a large target for light scattered along the path to the detector. Such large targets collect more light at forward scattering angles, thus reducing the attenuation effect. Such a geometry, however, produces broad angular weighting functions for the scattering measurement. These can be desirable for trying to resolve integrated backscattering, where, for a sufficiently compact sensor with broad source and detector beams, the attenuation effect can be negligible and thus be virtually ignored. However, when resolving $\beta(\theta)$ at fine angular increments, narrow weighting functions are necessary, which require relatively narrow source and detector beams, which will increase ε. For such sensors, the attenuation effect requires full correction (Twardowski et al., 2012).

6.4 Derivation of b_b from VSF measurements at single or multiple angles

For a single measurement of the VSF in the backward direction, b_b can be estimated using a conversion coefficient, termed a χ factor, for that measurement geometry. The χ factors are based on both modeled and/or measured VSF shape analysis in the backward direction (Oishi, 1990; Maffione and Dana, 1997; Boss and Pegau, 2001; Chami et al., 2006; Berthon et al., 2007; Sullivan and Twardowski, 2009) and generally must assume a constant shape in the particulate phase function in all water types unless the weighting function response of the VSF measurement approximates the $\sin(\theta)$ dependence in the integration of $\beta(\theta)$ to obtain $b_b\,(=\,2\pi\int_{\pi/2}^{\pi}\sin(\theta)\beta(\theta)\,d\theta)$ (Haubrich et al., 2011). Note that as the weighting function becomes broader in the backward direction, the calculation of b_b becomes less susceptible to changes in the shape of the phase function. Sullivan and Twardowski (2009) found a remarkable consistency (<5% RMSE deviation) in shapes of particulate phase functions in the backward direction using a dataset consisting of over three million VSF measurements collected throughout a wide variety of both coastal and oceanic environments (Fig. 6.3(A), Table 6.1). Specifically, they found

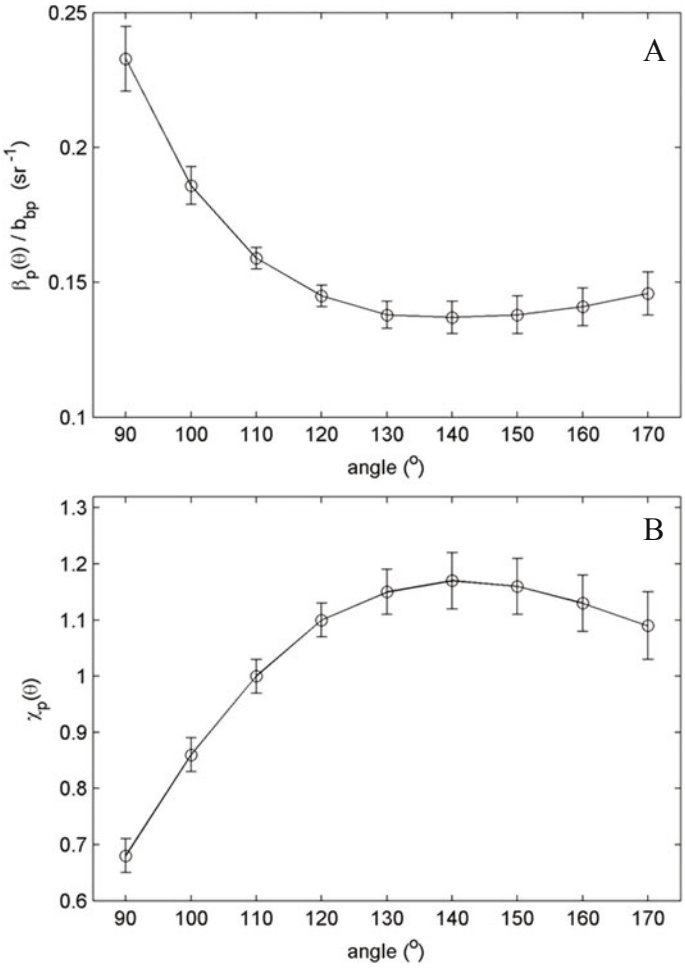

Fig. 6.3. The average (circles) and standard deviations (error bars through circles) of particulate phase functions (Fig. 6.3a) and χ_p factors (Fig. 6.3b) in the backward direction (adapted from Sullivan and Twardowski, 2009). The phase function and χ_p values represent the average of some three million VSFs measurements from a number of both coastal and oceanic environments

the minimum in the angular variability of the particulate VSF in the backward direction was between 110° and 120° (∼2% RMSE deviation), while the maximum variability at other angles was 5% or less. These *in situ* measurements were consistent with the original modeled results of Oishi (1990). Comparisons of the Sullivan and Twardowski (2009) average particulate phase function ($\lambda \sim 658$ nm) to a number of other particulate phase functions in the backward direction are shown in Table 6.1. These phase functions are from *in situ* measurements (Petzold, 1972; Boss and Pegau, 2001; Chami et al., 2006; Berthon et al., 2007), analytical models (Fournier and Forand, 1994) and laboratory-based phytoplankton culture studies (Whitmire et al., 2010). All values were normalized to the backscattering coefficient

Table 6.1. The average (avg.) and standard deviation as percent (σ %) of particulate phase functions in the backward direction, $\beta_p(\theta)$ / b_{bp}, from Sullivan and Twardowski, 2009 (ST), Fournier and Forand, 1994 (FF), Petzold, 1972 (P), Boss and Pegau, 2001 (BP), Berthon et al., 2007 (B), Whitmire et al., 2010 (W) and Chami et al., 2006 (C). All measurements were normalized to the backscattering coefficient with the contribution of the backscattering by water removed

Source	Angle: (°)	90	100	110	120	130	140	150	160	170
ST	avg.	0.233	0.186	0.159	0.145	0.138	0.137	0.138	0.141	0.146
	σ%	5.2	3.8	2.5	2.8	3.6	4.4	5.1	5.0	5.5
FF	avg.	0.235	0.185	0.157	0.143	0.138	0.139	0.143	0.148	0.152
	σ%	8.0	4.8	1.7	1.1	3.4	5.1	6.3	7.0	7.3
P	avg.	0.232	0.185	0.159	0.148	0.137	0.131	0.133	0.150	0.169
	σ%	4.4	1.9	2.5	4.0	5.1	3.3	2.9	3.7	13.1
BP	avg.	0.224	0.177	0.155	0.142	0.136	0.135	0.141	0.159	0.257
	σ%	4.3	2.5	3.1	4.2	3.3	3.5	4.2	6.4	34.8
B	avg.	0.226	0.182	0.156	0.142	0.138	0.140	0.144	0.152	0.174
	σ%	3.7	2.6	1.0	2.6	2.1	1.8	4.2	3.0	6.4
W	avg.	0.238	0.192	0.152	0.140	0.128	0.129	0.136	0.164	0.155
	σ%	7.9	14.9	7.8	9.4	10.6	11.1	12.9	14.8	32.4
C	avg.	0.189	0.155	0.135	0.123	0.123	0.132	0.147	0.169	0.227
	σ%	5.2	4.5	5.3	5.5	5.4	5.1	5.3	5.8	11.5

with the contribution of backscattering by water removed (i.e. $\beta_p(\theta)/b_{bp}$). The Petzold (1972) values are the average of his three turbid (San Diego Harbor, USA) measurements ($\lambda \sim 520$ nm). This average Petzold phase function is commonly used in radiative transfer modeling studies (e.g. Gordon, 1993; Mobley, 1994). The Boss and Pegau (2001) values are average data from both field measurements off coastal New Jersey and Mie modeling ($\lambda \sim 555$ nm). The Chami et al. (2006) values are average measurements from the Black Sea ($\lambda \sim 555$ nm), while the Berthon et al. (2007) values are the average of measurements from three different seasons in the northern Adriatic Sea ($\lambda \sim 510$ nm). The range of values of the two inputs of size distribution slope (assuming power law) μ and refractive index n_p for the Fournier–Forand modeled phase functions were between 3 and 4 (at 0.1 increments) for μ, and between 1.02 and 1.18 (at 0.02 increments) for n_p, and the value here is the average of this array output. This input array range (i.e. PSD slopes between 3 and 4, and refractive indices between 1.02 and 1.18) is a good representation of the ranges found in most natural waters (Twardowski et al., 2001; Sullivan et al., 2005; Jonasz and Fournier, 2007). Finally, the Whitmire et al. (2010) values are the average of phase functions from twelve different phytoplankton cultures, representing a wide diversity of size and shape ($\lambda \sim 555$ nm). Except for the values of Chami et al. (2006), the remaining particulate phase functions are within 5% of each other, except at 170°. We should note here that making accurate VSF measurements in the near back angles (170° to 180°) can be difficult owing to internal reflection issues in some instrument designs (Berthon et al., 2007; Sullivan and Twardowski, 2009). However, even with a small increase in the natural variability in the par-

ticulate phase functions in the near backward direction, given the $\sin(\theta)$ weighting in the integration to obtain b_b, this uncertainty will have a minimal effect on the accuracy of the b_b estimate. Similar to the Sullivan and Twardowski (2009) results, the percent variability in the average of these particulate phase functions has a minimum between 110° and 120°. These data strongly suggest that the assumption of constant shape and spectral independence for natural oceanic particulate phase functions (and the use of representative χ factors) is reasonable for most oceanic environments (see section 6.5.6 for further discussion).

As suggested by Boss and Pegau (2001), when using a χ conversion factor, the contribution to the total VSF measurement (β_t) by pure seawater (β_{sw}) should first be removed to yield particulate VSF measurements, β_p, (i.e. $\beta_p = \beta_t - \beta_{sw}$). Backscattering by pure seawater can be assumed constant with a very different phase function shape relative to natural particle populations. The values of Zhang et al. (2009) for $\beta_{sw}(\theta)$ and the backscattering coefficient of pure seawater (b_{bw}), with dependencies on temperature and salinity and a depolarization ratio of 0.039, are expected to be the most accurate at this time. Particulate conversion factors (i.e. χ_p, Fig. 6.3(B) and Table 6.2a) can then be used to estimate the particulate backscattering coefficient (b_{bp}) according to:

$$b_{bp} = 2\pi\, \chi_p(\theta)\, \beta_p(\theta)\,.$$

Averaged values of χ_p in the range $\pi/2$ to π must equal 1. The χ_p function must be convolved with a sensor's angular weighting function to derive a χ_p for that specific VSF measurement (see Table 6.2b for example). The total backscattering coefficient, b_b, can be determined by adding back in the contribution from pure seawater as a backscattering coefficient (i.e. b_{bw}).

Table 6.2a. The average (avg.) and standard deviation (σ) of χ_p factors from Sullivan and Twardowski (2009)

Angle: (°)	90	100	110	120	130	140	150	160	170
avg.	0.684	0.858	1.000	1.097	1.153	1.167	1.156	1.131	1.093
σ%	0.034	0.032	0.026	0.032	0.044	0.049	0.054	0.054	0.057

Table 6.2b. The Sullivan and Twardowski (2009) χ_p factors convolved with the weighting functions at the centroid angles for the ECO-VSF (104°, 130° and 151°) and ECO-BB (124°) sensors

ECO centroid angle θ(°)	104	124	130	151
$\chi_p(\bar{\theta})$	0.89	1.076	1.104	1.138

For multiple VSF measurements in the backward direction where the shape of the VSF is adequately resolved, the VSF can be simply integrated to provide b_b. Where only a few measurements are made over different angular ranges, b_b can be obtained by integrating over a polynomial fit to the available data. For example,

using a backscattering sensor measuring the VSF at centroid angles 100°, 125°, and 150°, Sullivan et al. (2005) used the following steps to derive b_{bp}. First, the three $\beta_p(\bar{\theta}_i)$ measurements were multiplied by $2\pi \sin(\bar{\theta}_i)$ to add the weighting of the spherical integration. Since $2\pi \sin(\pi) = 0$, four values in the backward hemisphere could be used in the fitting procedure with a regression anchor of zero at 180°. The resulting values were then fit with a third order polynomial and integrated from $\pi/2$ to π (90° to 180°) to yield b_{bp}.

We should note here a recently described method to measure b_b that is not dependent on single (or multiple) angle VSF measurements (i.e. Haubrich et al., 2011). These authors have designed a relatively simple instrument that produces a $\sin(\theta)$ weighting function by using a circular detector aperture surrounding the optical axis of the source beam exit window. Theoretical analysis has shown that b_b may be resolved with a maximum uncertainty of only a few percent and potentially <1 percent with this technique. To date, this instrument is not yet commercially available.

6.5 Analysis of measurement uncertainties

Uncertainties in backscattering measurements can arise from multiple sources, including reproducibility in sensor machining and components, calibrations, instrument wear and age, and environmental dependencies due to ambient temperature, light, and fluctuations in electromagnetic interference. These factors can affect measurements in two ways: by introducing uncertainties in the sensor's baseline response (i.e., a change in the detector background dark offset D), or by introducing uncertainties in the sensor's dynamic response (i.e., a change in the effective calibration scaling factor f). Since the background dark offset is nominally a constant, the significance of any long-term dark offset drift to measurement uncertainties will be dependent on the optical environment where the sensor is deployed; that is, it will have the greatest effect in clear, low scattering environments where the *in situ* signal will be small. On the other hand, changes in the dynamic response (scaling factor) will not be dependent on the optical environment. Scaling factors are multiplicative, so percent changes directly impact uncertainties defined in terms of percent.

6.5.1 Calibration

Uncertainty in calibration arises from assumptions made in the numerical computation of the angular weighting function, the input parameters for calculation of bead phase functions using Lorenz–Mie theory, and the methodological reproducibility for the laboratory measurements. With respect to the weighting function, accuracy is dependent on how close the geometric variables used in the numerical analysis match that of the actual sensor. For sensors with well-defined detector FOVs, with precisely set apertures and source beams that are well-behaved such as a laser, weighting function accuracy is expected to be excellent. The numerical analysis described here has been validated experimentally in such a system (Twardowski et al., 2012). For sources such as LEDs that can exhibit uneven intensity distributions and variability from LED to LED, weighting function accuracy is more difficult to

evaluate. In such cases, accuracy can be assessed by replicating the calibration with multiple bead sizes to determine to what extent resultant scaling factors agree (they should be identical). Note this check evaluates the uncertainties of the complete calibration, not just the weighting function (see below). The uncertainty associated with weighting functions can be minimized by using bead sizes in calibration that have as flat a response in the backward direction as possible. Phase functions typically flatten as bead sizes decrease. For example, the phase function for 0.2 μm beads is nearly constant at 650 nm at angles greater than about 100°.

The Lorenz–Mie theory computation of phase functions requires the size distribution and complex refractive index of the bead dispersion. NIST-traceable polystyrene beads (ThermoScientific Inc.) are high quality and suitable for calibration. In terms of impacting the shape of the phase function, mean diameter is typically much more important than the standard deviation of the distribution. For beads with nominal mean diameter of $0.2 \pm 2\%$ μm (ThermoScientific catalog number 3200A), maximum possible uncertainties in phase function shape are observed in the near-backward at around 5%. For beads with nominal mean diameter of $2.0 \pm 1\%$ μm (ThermoScientific catalog number 4202A), maximum possible uncertainties in phase function shape are also observed in the near-backward at around 5%. As the angular weighting function becomes broader in the backward, this maximum possible uncertainty decreases substantially.

For the real refractive index of the polystyrene beads, several dispersion models have been published (Matheson and Saunderson, 1952; Nikolov and Ivanov, 2000; Ma et al., 2003). Values provided by Duke Scientific (now ThermoScientific) are considered the most accurate as these values provide theoretical attenuation spectra that closely match hyperspectral measurements. Using the Cauchy dispersion equation:

$$n_p = A + \frac{B}{\lambda^2} + \frac{C}{\lambda^4}\,,$$

with λ in μm, the Duke Scientific values are $A = 1.5663$, $B = 7.85 \times 10^{-3}$, and $C = 3.34 \times 10^{-4}$. Uncertainties in the red portion of the visible are an estimated ± 0.001. The significance of refractive index uncertainty increases dramatically as bead size increases. For 0.2 μm beads, a 0.005 difference in refractive index only leads to a 0.2% maximum difference in phase function values in the backward direction. For 2 μm beads, the maximum phase function difference increases to 8%. For 25 μm beads the difference increases to >50%. This substantial uncertainty is strong justification for using small bead sizes in calibrations. Ma et al. (2003) is the only study to experimentally determine the imaginary portion of the refractive index n_i. From 370 to 700 nm, n_i ranged between 0.0003 and 0.0005, with a value of 0.0005 ± 0.0001 in the red. This uncertainty has a negligible impact on phase function shapes for both 0.2 μm and 2 μm beads. As stated previously, using the bead manufacturer's reported value for the real part of the refractive index and Ma et al., (2003) for the imaginary part is recommended. Further, for calibrations of sensors with blue or green wavelengths, 0.1 μm beads should be used in preference to 0.2 μm beads, as the phase function of 0.1 μm beads is flatter in these wavelength regions. The drawback to using 0.1 μm beads is higher concentrations of beads are required to get an adequate dynamic range in signal, and the beads are costly, thus 0.2 μm beads are generally preferred for red wavelength sensor calibrations.

ThermoScientific uses a variety of techniques to certify the reported diameter and distribution of their beads including optical microscopy with a NIST calibrated stage micrometer, electron microscopy, electrical resistance analysis, and photon correlation spectroscopy. Our laboratory has validated some of the reported size distributions with scanning electron microscopy. It is important to note that the primary application of these beads is to provide a size calibration for particle sizing devices. The critical parameter is the location of the distribution peak, or modal (also mean) diameter, and this is what is NIST certified. Such beads are not NIST certified as standards for the calibration of scattering sensors. While they still may serve this application effectively (and we think they do), a concern may be that, unlike many single particle size analyzers, all the particles potentially present in the bead solution influence bulk scattering in the calibration of volume scattering sensors. Contaminating particles larger than the bead size are probably not a significant contributor but small colloidal particles that are not detected by many of the validation methods above could be present. These particles have low scattering efficiencies, but their concentration is unknown and might be relatively high. Manufacturing pure water without any particulate contamination that may influence optical scattering is extremely difficult (Morel, 1974). The assumption is that the population of beads in the prepared solution would be in such high concentrations as to effectively render any contamination negligible. Because of their very small size, contamination is likely less a problem with bead distributions peaking in the submicrometer size range.

All laboratory procedures involved in the VSF and b measurements for the solutions of beads are subject to methodological errors in replication. In practice, if several calibration points are collected for a least-squares linear fit with careful attention to detail, the methodological uncertainty for the slope determination is ~1% (RMSE). Experimental calibration replication confirms these uncertainties.

6.5.2 Instrument resolution and electronic noise

Resolution and noise will be a function of optical components used and electronics. Commonly used optical components for backscattering measurements are LED sources and silicon photodiode detectors (Maffione and Dana, 1997; Moore et al., 2000; Twardowski et al., 2005). To assess uncertainties for a practical sensor embodiment, in this section and the following sections, we will consider the WET Labs (Philomath, OR, USA) ECO backscattering sensors. Sensor design geometry and associated angular weighting functions for ECOs are shown in Figs. 6.4 and 6.5(A), respectively.

WET Labs ECO sensors employ a 12-bit A/D converter, providing a 4096 count dynamic range. For a standard sensor, with electronic noise levels tuned to approximately 2 digital counts, resolutions of about 2×10^{-5} m^{-1} sr^{-1}, 8×10^{-6} m^{-1} sr^{-1}, and 4×10^{-6} m^{-1} sr^{-1}, are obtained with the ECO-BB sensor for blue, green, and red LED source measurements, respectively. Sensors can be tuned to higher or lower dynamic range. At all wavelengths, this resolution is 7–8% of the volume scattering of pure seawater, which is similarly strongly dependent on wavelength (Zhang et al., 2009). Improving resolution with increasing wavelength is a function of increasing LED power output and resulting scattered signal power.

The dynamic range of ECO sensors is also consequently wavelength dependent, where, with noise levels tuned to 2 digital counts, typical signal saturation for blue, green and red wavelength ECOs occurs in natural waters with b values of roughly $20 \pm 5\,\mathrm{m}^{-1}$, $10 \pm 5\,\mathrm{m}^{-1}$, and $5 \pm 1\,\mathrm{m}^{-1}$, respectively.

6.5.3 Long-term stability in background dark offsets (baseline noise)

Dark offsets are relatively straightforward to measure for WET Labs ECO sensors, so large amounts of data on offsets are available with which to assess long-term stability. Offsets are determined by completely covering the detector with opaque tape, leaving the light source fully exposed, and immersing the sensor in water. Measurements of dark offsets are taken over an appropriate time period (e.g., 1 min.) to determine both the average signal (D) and the variability about the average. Routine monitoring of dark offsets, especially during field deployments, is recommended, as it may reveal unanticipated variations due to specific instrumental/power setups and environmental conditions (Twardowski et al., 2007). For the highest accuracy, dark offsets should be measured *in situ*.

Sensor components affecting dark offsets are the silicon photodiode detector and associated electronics. Dark offsets have been found to be very stable over long time periods (years). For example, Dall'Olmo et al. (2009) recorded ECO dark offsets every other day during a one-month cruise and found they varied by ±1 count

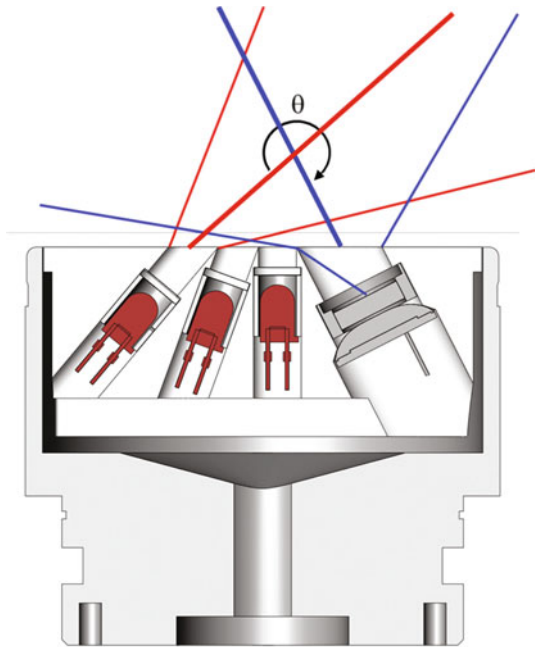

Fig. 6.4. Schematic drawing of an ECO-VSF sensor optical head measuring the VSF at three different geometries. Centroid angles of the measurements are at 104°, 130° and 151°. Three LED sources (shaded red) and a photodiode detector are shown, with an interference filter above the dome-shaped photodiode detector. Sketches of the beams for the 104° measurement with sources in red and detector FOV in blue are shown

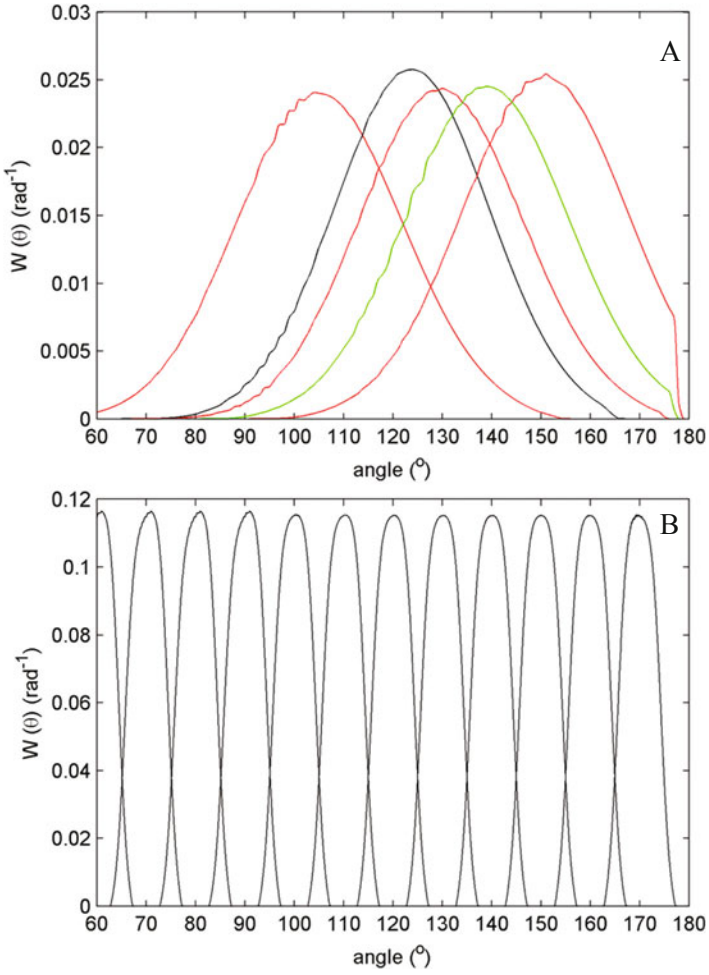

Fig. 6.5. (A) Numerically derived weighting functions, W $(\bar{\theta})$, for the WET Labs ECO-BB (black line), ECO-NTU (green line), and ECO-VSF (red lines) sensors. Centroid angles are 124° for the ECO-BB, 140° for the ECO-NTU, and 104°, 130° and 151° for the ECO-VSF. Centroid angles are simply the maximum of the weightings; other methods of computing centroid angles, such as finding the mid-angle in the weighting distribution, agree to within a degree. (B) Numerically derived W $(\bar{\theta})$ for each of the centroid angles of the WET Labs MASCOT VSF device over the same angular range

(less than the tuned resolution of the measurement). Additionally, dark offsets from two different ECO sensors (an ECO-VSF and ECO-BB3) were tracked over 6 and 8 years, respectively, by this research group during extensive field use and found to have rarely varied greater than ±2 counts from the original factory determinations. Most of these dark offsets were recorded *in situ* before ambient measurements, in waters ranging in temperature from 1°C to 30°C. Laboratory tests have confirmed the lack of any dependence in dark offsets with ambient temperature (see

section 6.5.5.2). However, in rare instances (<0.1% of available data), dark offset determinations for both sensors were temporarily found to be 5 to 6 counts lower than normal. This drift may be due to a very rapidly changing thermal environment or a period of unique electromagnetic interference (such as a grounding or power system resistance problem), although the effect has not been reproducible in the laboratory.

6.5.4 Long-term stability in scaling factors

Scaling factors are a function of the source output and the dynamic response of the detector assembly. Any physical damage or fouling of the sensor face affects both components. Scratching of the source or detector windows may impact the transmittance of light through the sensor–water interface, especially if the difference in refractive index between the windows and water is large. Scratching may also alter the weighting function of the measurement. Depending on the sensor design, fouling of the sensor face can artificially increase or decrease the measured scattering signal. If the source and detector are far enough apart, the scattering signal will decrease. If the source and detector are very close, source light can scatter through the surface film directly into the detector, causing an artificial signal increase.

Sources of long-term drift due to changes in source intensity output, detector dynamic response and optical component degradation (e.g. interference filters) are difficult to quantify separately and are sensor and situation specific. However, assuming a clean and undamaged sensor, tracking the difference in scaling factors obtained through recalibrations over time should yield some indication of their cumulative magnitude. This type of analysis was conducted with ten different WET Labs ECO sensors of various designs and age. Although this was not a rigorous, long-term analysis (for example, drifts were not normalized to hours used), scaling factors in ECO sensors increased by about 8% y^{-1} for blue wavelength sensors, 1–2% y^{-1} for green wavelength sensors, and 3–4% y^{-1} for red wavelength sensors (Fig. 6.6(A)). For most of the ECO sensors studied, only two calibration points were available, and most calibrations were only 1 to 2 years apart, which is obviously not ideal for detailed characterization. However, a more extensive scaling factor calibration history, available from a red wavelength ECO-VSF, exhibited what is likely the shape function of long-term scaling factor drift. In this case, five calibrations were done approximately once per year over five years. The results reveal that the drift approximates a first-order exponential increase with time (Fig. 6.6(B)). This characteristic shape likely indicates that gradual dimming of LEDs with age is the causative mechanism, as LEDs are known to exhibit decreases in light output with age. The rates of drift for blue LED sensors appeared higher than those of green and red LED sensors. It is theorized that these higher drift rates may also include a 'yellowing' effect from the optical epoxy that is used in potting the optical components in the sensor face. Experiments are currently underway to test this theory.

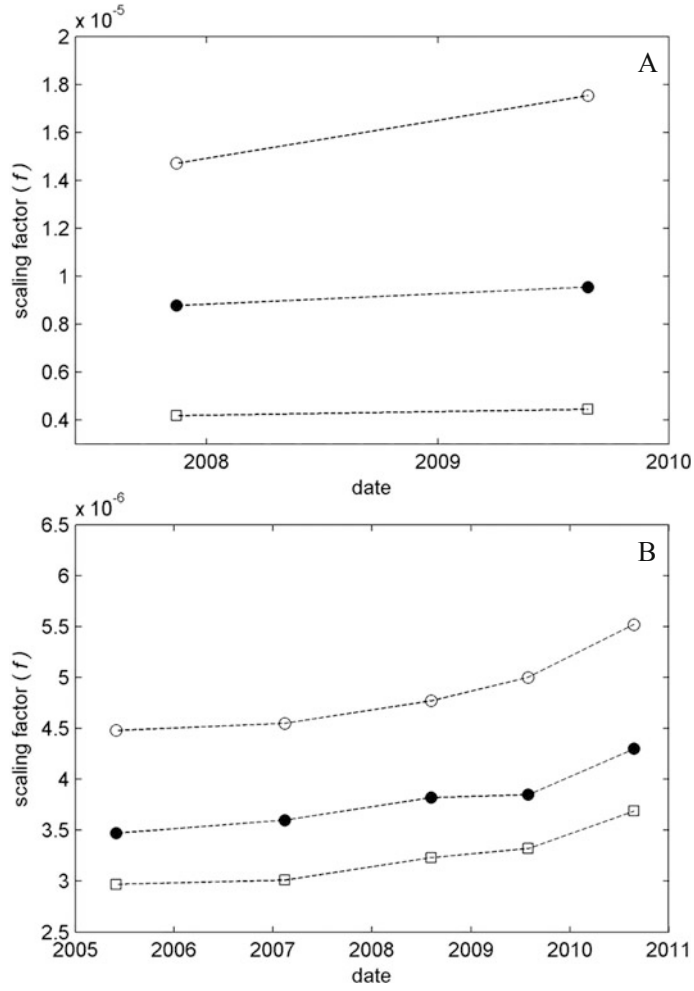

Fig. 6.6. (A) The change in calibration scaling factors (f) as a function of time for a representative ECO-BB3 sensor. The blue wavelength channel f (open circles) increased by about 10% y^{-1}, the green wavelength channel f (filled circles) by about 4% y-1. and the red wavelength channel f (open squares) by 3% y^{-1}. (B) The change in f as a function of time for a red wavelength ECO-VSF sensor. Overall, the three centroid angles, 104° (open circles), 131° (filled circles) and 151° (open squares) all increased by about 4% y^{-1}; however, the rate of change in f is increasing with time

6.5.5 Environmentally induced uncertainties

Along with the methodological uncertainties and long-term drift described above, evaluating sensor performance under different environmental conditions parameterizes short-term stability. Common environmental factors that could affect sensors include changes in ambient temperature and light, and electromagnetic interference (EMI). Each of these factors is addressed below for the WET Labs ECO sensors.

6.5.5.1 Ambient light

For ECO sensors, control electronics synchronize each individual LED light source with the photodiode detector at 60 Hz to reject ambient light. Ambient light is directly detected by control circuitry and removed from the LED source signal using electronic filtering. Since the filtering algorithm subtracts ambient light from the available signal range, the sensor's dynamic range is reduced when ambient light is present. Ambient light rejection is very robust as long as the sensor is oriented in a downward or horizontal direction. Upward-looking sensors (used on special autonomous platforms, e.g. Sullivan et al., 2005, 2010) could be subject to ambient light saturation in the upper few meters of surface waters.

6.5.5.2 Temperature

To examine photodiode detector temperature stability, dark offsets were continuously measured in over thirty ECO sensors as the temperature was slowly cycled over a 12-hour period through the typical oceanic extremes of 2°C to 35°C. A representative result for these sensors is shown in Fig. 6.7(A). Of all sensors tested, a few exhibited small irregularities, where an increase or decrease of several dark offsets at temperatures >30°C was observed, equal to a 1% to 2% variation in the baseline dark counts. Overall, however, these experiments indicate that sensor detectors and associated electronics appear extremely stable (<1% drift) over oceanic temperature extremes.

A well known characteristic of LEDs is that the intensity of light from these sources decreases with increasing temperature (Hewlett Packard, 1995). Depending on the semiconductor materials used in construction, red LEDs tend to be more sensitive to temperature-intensity effects than blue and green LEDs. A red wavelength ECO-VSF (6 years old) was exposed to a heating and cooling cycle over the 2°C to 35°C range. The percent change in LED intensity (via LED reference signal) was 10% over the full temperature range (Fig. 6.7(B)). Similar experiments with blue and green wavelength ECO sensors found little to no LED temperature dependency (2% or less over the entire temperature range). Other tests with instruments containing LED sources have confirmed these results. As the ECO sensors were calibrated around 20°C, blue and green wavelength ECO sensors would be expected to have little to no temperature uncertainty under normal or even extreme oceanic conditions, while red wavelength ECOs could have up to 5% uncertainty if operated at either temperature extreme. If an instrument is going to be routinely used in environments at the extremes of the oceanic temperature range, scaling factor calibrations should be conducted as close to the expected environmental temperature as possible for highest accuracy.

Note that temperature is also known to have an effect on LED peak spectral output, typically increasing (with increasing temperature) from 0.03 to 0.13 nm per °C, depending on LED semiconductor material (Reynolds et al., 1991). Thus, a 2 to 3 nm shift in LED peak spectral output could occur over the entire oceanic temperature range. Since ECO sensors typically employ bandpass interference filters in the 20 to 30 nm FWHM range, source output intensity should not be affected.

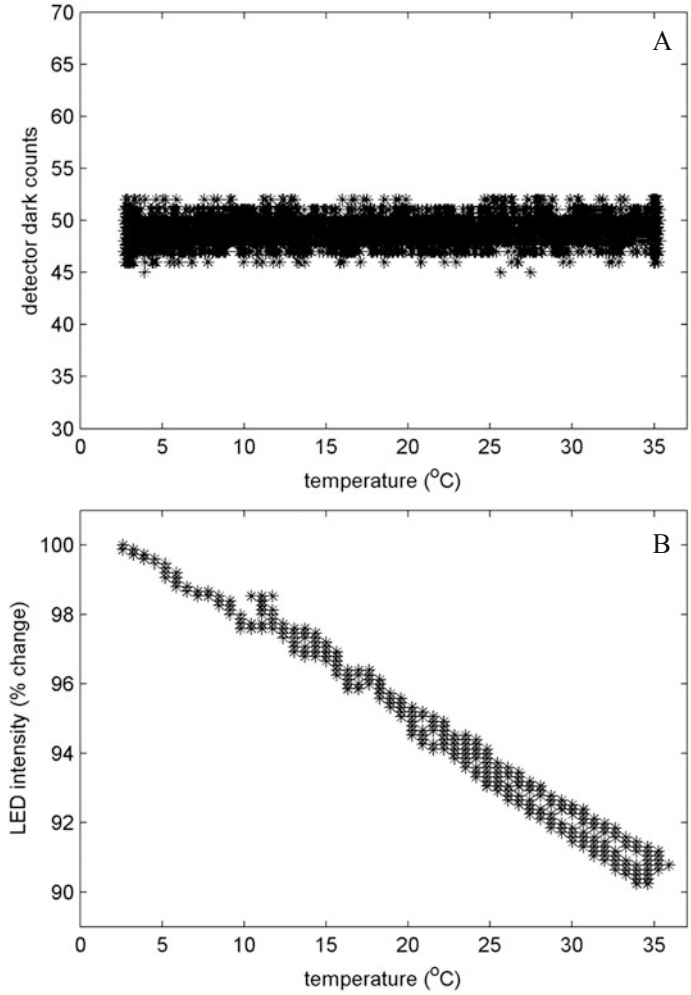

Fig. 6.7. (A) The typical response of detector dark offset as a function of temperature for an ECO sensor. (B) The percent change in light intensity as a function of temperature for a red wavelength LED in an ECO sensor

6.5.5.3 Electromagnetic interference (EMI)

Electromagnetic interference (EMI) is a common concern for sensors deployed in conductive seawater. ECO testing has shown vulnerability to external noise from other oceanographic instruments (e.g. pumps, other sensors, etc.) depending on deployment characteristics and system setup. Causes of the EMI have been linked to poor system grounding, stray voltage leaks and/or RS-232 frequency coupling. Typically, the interference may increase the standard deviation of detector signal up to a factor of 2 to 3, although the increased EMI does not change the averaged measurement value (i.e. the noise is normally distributed). Improved shielding in

sensors and associated cables can reduce EMI noise substantially (50%). Since EMI is a white noise effect, measurement reproducibility is unaffected.

6.5.6 Conversion coefficient (χ factor) uncertainties

The review in this section has, to this point, dealt with uncertainties associated with sensor output in terms of the VSF (β), focusing on the WET Labs ECO example. However, as detailed in section 6.4, estimating the b_b using any sensor's single VSF measurement requires using a conversion coefficient (χ factor) for that angle. As mentioned, the key assumption in using a single set of χ factors to estimate accurate b_b values is that there is minimal variability in the shape of the particulate phase function for the chosen VSF measurement geometry, a condition which relaxes somewhat as the weighting function broadens. This assumption was verified by Sullivan and Twardowski (2009), in agreement with theoretical models and past field measurements (Oishi, 1990; Maffione and Dana, 1997; Boss and Pegau, 2001; Chami et al., 2006; Berthon et al., 2007). Sullivan and Twardowski (2009) concluded that under most oceanic conditions, estimates of b_b using a suitable scattering angle and χ factor should have a maximum uncertainty better than a few percent. Both Boss and Pegau (2001) and Sullivan and Twardowski (2009) have also suggested that χ values should be spectrally independent for natural oceanic waters. This has been examined both theoretically and experimentally, where in most cases, the shape of the particulate phase function has been found to have little spectral dependency (e.g. Ulloa et al., 1994; Maffione and Dana, 1997; Boss and Pegau, 2001; Twardowski et al., 2001; Mobley et al., 2002; Vaillancourt et al., 2004; Berthon et al., 2007; Whitmire et al., 2007, 2010). However, it should be noted that in some cases, spectral variability in b_{bp}/b_p and χ_p has been observed (Chami et al., 2006; McKee et al., 2009). Chami et al. (2006) reported that χ_p varied spectrally $\pm 6\%$ for natural particle populations and up to $\pm 20\%$ in phytoplankton laboratory cultures, while McKee et al. (2009) reported finding 25% to 30% spectral variability in b_{bp}/b_p within mineral-rich coastal waters. Deviations from a spectrally independent phase function may occur, for example, in waters with steeply peaked size distributions. A majority of studies have confirmed the spectral independence, however. In addition to the Sullivan and Twardowski (2009) study, Berthon et al. (2007), using a later generation of the VSF instrument employed by Chami et al. (2006), found very little (1% to 2%) spectral dependency in natural particle populations in the Mediterranean Sea. Similarly, Whitmire et al. (2007) found spectrally independent b_{bp}/b_p in a diverse oceanic dataset containing measurements collected from five different regions around the world, while Whitmire et al. (2010) found no significant spectral variability in χ_p for twelve different phytoplankton cultures with a wide variety of shapes and sizes. Although more work is needed to better define those cases where the shape of the phase function may deviate from spectral independency, the majority of theoretical and experimental studies to date support the use of a single set of χ_p values for natural oceanic waters.

6.5.7 Measurement uncertainty summary

As a general rule, uncertainties in calibrating sensors measuring volume scattering in the backward direction decrease as bead size decreases. For 0.1-μm beads with a nearly flat phase function response in the visible spectrum in the backward direction (so that measurement geometry uncertainty is minimized), the only significant error in calibration is the 2% uncertainty in mean bead diameter, which results in a maximum possible uncertainty of 5% in the phase function shape near 180°. For broad weighting functions, this maximal uncertainty decreases, so, in practice, an uncertainty of about 2% would appear reasonable for sensors such as the WET Labs ECO. Propagated with an estimated uncertainty of about 1% in laboratory determinations of linear slope between raw sensor signal and total scattering b, resulting scaling factors have an expected uncertainty of 2–3%.

Using 2.0-μm beads in calibration will increase uncertainty because the phase function shape is not as flat in the backward and the uncertainty in bead refractive index may be as high as 8%. However, if we assume the Duke Scientific uncertainty in the red of 0.001 is reasonable, then the maximal uncertainty due to the real part of refractive index is only 3%. Propagating error, we thus may expect uncertainties in calibration with 2.0 μm beads to be 1–2% higher than that for 0.1 μm beads, but that does not include weighting function uncertainty that potentially becomes an issue because of the introduced variability in phase function shape with the 2.0 μm beads.

Because of the multiple sources of possible uncertainty in calibrations, and the difficulty in characterizing some uncertainties, independent validation provides a valuable check for the overall uncertainty in calibrations. This can be accomplished by (1) calibrating the same device multiple times with different bead size distributions to check for consistency in derived scaling factors and (2) intercomparison with other sensors that have similar and dissimilar measurement geometries. For various sensor geometries measuring volume scattering throughout the backward hemisphere, we have observed worst-case differences of 5% when the same sensor was calibrated with both 0.1-μm and 2-μm NIST traceable beads. For different sensors with the same measurement geometry calibrated with the same beads, worst-case agreement was also 5%. Intercomparison of sensors with different measurement geometries is addressed in sections 6.6 and 6.7.

The above discussion all relates to calibration with high-quality NIST traceable bead distributions. ThermoScientific and other manufacturers also sell non-NIST traceable bead products for size analyzer calibrations with mean diameter and standard deviation of the distribution reported on the bottle. However, the uncertainty in these distribution parameters is not known. Solutions of non-NIST traceable beads also are less purified than their NIST traceable counterparts, with up to an order of magnitude more background solids (Duke Scientific, now ThermoScientific, personal communication, 2006). Concentrations of beads in solution are also much higher, however. Nevertheless, comparison of scaling factors derived from calibrations with both NIST and non-NIST traceable 2.0 μm diameter beads have shown reasonable agreement with a worst-case error of 8% for WET Labs ECO sensors.

Long-term drift for ECO sensors appears to be driven by dimming of the LED source, with observed annual rates of drift approximately 8–10%, 1–2%, and 3–4%

for blue, green, and red LED sensor measurements, respectively, although these rates will be dependent on sensor usage. Annual sensor recalibration ensures green and red scattering measurements drift no more than a few percent, whereas blue scattering measurements would need to be calibrated more frequently to obtain a similar uncertainty. The only significant environmental effect for the ECO sensor was determined to be the temperature dependency of the red LED source, with a 10% change in response over the full temperature range expected for typical ocean conditions. Overall, the most stable ECO scattering measurements are made with green LED sources.

6.6 Sensor comparisons in the field

Comparing measurements of volume scattering from sensors with different optical components, beam geometries, resolution, and optical pathlengths can be a valuable way to evaluate assumptions in calibration. During a number of field efforts, the ECO-VSF and ECO-BB3 sensors discussed in section 6.5.2 were co-deployed with the WET Labs Multi-Angle SCattering Optical Tool (MASCOT) measuring the VSF at 658 nm over a $\bar{\theta}$ angular range extending from 10° to 170° in 10° increments (Fig. 6.5(B)). Details of the MASCOT, its use and calibration can be found in Sullivan and Twardowski (2009) and Twardowski et al. (2012). The pathlength of the MASCOT is 20 cm for each channel, much longer than that of the ECO sensors, and requires a more exact attenuation correction (Twardowski et al., 2012). The MASCOT uses a 30-mW laser diode source, has a 14-bit dynamic range, and samples at 20 Hz. Estimated accuracy in VSF measurements with MASCOT are 2% to 3%. The spectral centroid of the ECO-VSF and the red LED channel of the ECO-BB3 were within 1 nm of the MASCOT's. All sensors were calibrated with 0.2-μm NIST traceable beads.

Measurements from all three sensors were collected in a wide variety of water types from five different coastal and oceanic environments: off the coast of Oahu, Hawaii, during March of 2007; the New Jersey bight during May of 2007 and July of 2008; the Santa Barbara Channel off the coast of Santa Barbara, California, during September 2008; and the Ligurian Sea off Liguria, Italy, during October of 2008. Collectively, these measurements represented over 5 000 one-meter binned VSF samples from vertical profiles taken at each of the locations. Comparative measurements of β_p from the three sensors were very similar over a large dynamic range of VSFs (Fig. 6.8(A)).

The mean β_p values from all field measurements show that the ECO-VSF and ECO-BB3 were 5% to 10% higher than those of the MASCOT interpolated at their specific centroid angles (Fig. 6.8(B)). However, while ECOs resolve angular scattering in the backward direction with relatively broad source beams and detector FOVs (large $\Delta\theta$ for W) to minimize uncertainties in deriving backscattering coefficients from a single measurement (i.e. Fig. 6.5(A)), the MASCOT angular weighting functions are more discrete (small $\Delta\theta$ for W) (i.e. Fig. 6.5(B)). Results are thus not directly comparable unless the MASCOT VSF is appropriately weighted to the ECO geometry:

$$\beta(\bar{\theta}_{ECO}) = \int_0^{\pi} \beta_M(\theta) W_{ECO}(\theta)\, d\theta\,,$$

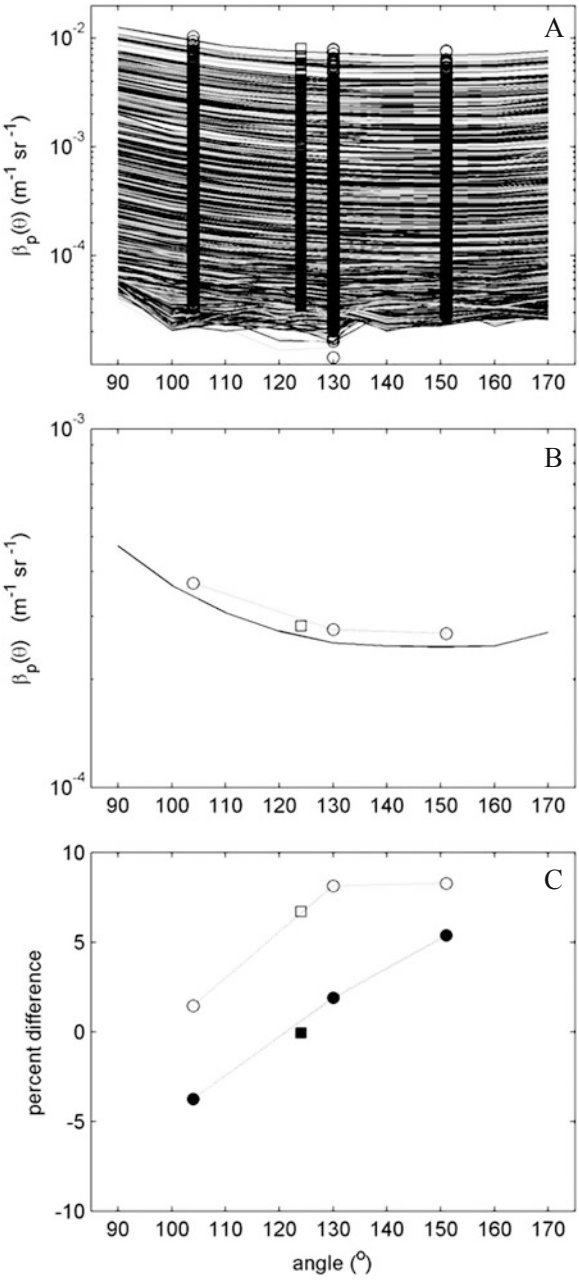

Fig. 6.8. (A) The VSFs in the backward angles from all field sites (see text) for the MASCOT (solid lines), ECO-VSF (open circles) and ECO-BB3 (open squares). (B) The average values of all field data for the MASCOT (solid line), ECO-VSF (open circles) and ECO-BB3 (open square). (C) The percent difference for the ECO-VSF (circles) and ECO-BB3 (square) relative to the MASCOT measurements before convolving the averaged MASCOT VSF with the ECO weighting functions (open symbols) and after (filled symbols)

where $\bar{\theta}_{ECO}$ is the centroid angle of the ECO weighting function, $\beta_M(\theta)$ is the MASCOT VSF, and $W_{ECO}(\theta)$ is the ECO weighting function. After convolving the MASCOT VSF data to the ECO weighting functions, the three independent instruments agreed to within ±5% (Fig. 6.8(C)). The difference between the sensor's measurements at centroid angles 124° and 130° were the lowest (<2% difference) and were higher (5%) at 104° and 151°, suggesting that the most accurate calibrations are attainable at centroid angles near the middle of the backward. Since the ECO measurement centered at 104° includes some forward scattering where the VSF shape in natural waters starts to increase rapidly, any uncertainty in the shape of the weighting function in this region becomes amplified. For the measurement centered at 151°, uncertainty in the VSF shape and the ECO weighting function in the range 170° to 180° could both contribute to the small disagreement. It should be noted that very similar differences have been observed between the MASCOT and other ECO sensors at the same angles, indicating that these differences are non-random.

Direct *in situ* comparisons of backscattering estimates from ECO sensors and other commercial devices that have a similar design concept, but use different centroid angles, weighting functions, calibration procedures (e.g. 'plaque method'; Maffione and Dana, 1997) and methods to estimate b_b, have agreed within 10% or better. For example, Loisel et al. (2007) found that ECO and Hydroscat^{TM} (HOBI Labs, Tucson, AZ, USA) sensors agreed to within a few percent during co-deployments in the English Channel and North Sea. These comparison measurements were taken over a large range in b_b from ∼0.003 to 0.06 m^{-1}. Similarly, Boss et al. (2004a,b) found the instruments agreed to within ∼2% in co-deployments off the coast of New Jersey, while Twardowski et al. (2007) found agreement between the two sensors within 3% from measurements in very clear South Pacific waters. McKee et al. (2009) reported that in UK coastal waters, ECO and Hydroscat measurements agreed within 10%, while Chami et al. (2005) reported a similar agreement between the sensors in Black Sea deployments. Boss et al. (2007) found that ECO and Hydroscat sensors agreed to within 3% in co-deployments in Crater Lake, OR, an optically clear and deep (∼600 m) sub-alpine lake. During measurements off coastal New Jersey, Boss et al. (2004a,b) found that comparisons between an ECO sensor and the Volume Scattering Meter (VSM) (Lee and Lewis, 2003), an instrument capable of VSF measurements from ∼0.6° to 177° in 0.3° increments, agreed within 10% or better. A comparison between VSM, ECO and Hydroscat measurements taken during the summer of 2000 at the LEO-15 coastal observatory site reported that sensors agreed within 8% (Mobley et al., 2002). Balch et al. (2009) found that in both laboratory and field measurements, an ECO-VSF agreed within a few percent of the values from an EOS light scattering photometer (Wyatt Technologies Corp., Santa Barbara, CA, USA), a bench-top VSF instrument capable of measurements from 10° to 170°. While these sensors compare very well in side-by-side measurements, it is not surprising that there are small differences. Notably, even if all aspects of calibration, instrument age, measurement uncertainties, etc. are known and corrected in these data, differences in weighting functions alone, if not corrected for in the comparison, could result in several percent difference between sensor's $\beta(\theta)$ values.

6.7 Conclusions

Determining the backscattering coefficient requires measurement of the VSF in the backward direction at one or more angular weighting distributions. If the VSF is resolved at a sufficient number of angles, it may be simply integrated to provide b_b. With only a single VSF measurement in the backward, an approximation must be made, although this is expected to have excellent accuracy because of the remarkable consistency in the shape of the VSF observed for natural waters. Additionally, as the weighting function of the VSF measurement broadens in the backward, it will experience less dependence on changes in the shape of the particulate phase function. Theoretical analysis has shown virtually no expected dependence (<1%) on phase function shape in deriving b_b using a recently developed single measurement volume scattering geometry employing a $\sin(\theta)$ weighting (Haubrich et al., 2011).

With careful attention to detail in sensor design and construction, weighting function derivation, calibration bead choice, theoretical computation of phase functions for calibration beads, and laboratory measurements, uncertainties of 2% or better should be attainable. This is the uncertainty expected for a sensor such as the MASCOT discussed in the previous section (Twardowski et al., 2012). For sensors such as the ECO that use broad weighting functions with LED sources that may exhibit some variability in the distribution of LED output intensity, uncertainties may be as high as 5%, assuming recent calibration. These estimated uncertainties were verified in sensor calibration replication and inter-comparisons of sensors using different measurement geometries and calibration methods. The lowest rates of temporal drift were observed for ECO measurements employing green LED sources. In addition to inter-comparisons of the MASCOT and ECO sensors (section 6.6), ECO sensor b_b values have been compared with values from other sensors with agreement within 10% and often better than 3% (e.g. Boss et al., 2004a,b, 2007; Chami et al., 2005; Loisel et al., 2007; Twardowski et al., 2007). Further validation of ECO backscattering measurements have been demonstrated through optical closure between *in situ* backscattering and passive solar reflectance measurements using radiative transfer computations (Mobley et al., 2002; Tzortziou et al., 2006; Twardowski et al., 2007; Gordon et al., 2009). Considering the small differences between the MASCOT and ECO sensors (Fig. 6.8(C)), a hopeful aspect is that these differences are non-random, indicating that further improvement is possible in the future by accounting for small bias error(s) that remain embedded in some aspect of calibration.

Acknowledgements

The authors would like to thank Scott Freeman, Heather Groundwater, Alex Derr, Cale Wetzel, Marvin Johnson, Wes Strubhar and Dan Morrissette for their assistance in collecting data for this review. We also thank David McKee, Emmanuel Boss and Alexander Kokhanovsky for helpful comments on the manuscript. We are grateful to acknowledge support for this work from ONR contracts N00014-06-C-0027, N000140510064, N0001405C0418, N00014-02-C-0173, ONR MURI grant N000140911054, NASA contract NNX09AV55G, and WET Labs.

References

Agrawal, Y. C., 2005: The optical volume scattering function: Temporal and vertical variability in the water column off the StateplaceNew Jersey coast, *Limnol. Oceanogr.* **50**, 1787–1794.

Balch, W. M., A. J. Plueddeman, B. C. Bowler, and D. T. Drapeau, 2009: Chalk-Ex–Fate of $CaCO_3$ particles in the mixed layer: Evolution of patch optical properties, *J. Geophys. Res.*, **114**, C07020.

Beardsley, G. F., Jr., H. Pak, K. Carder, and B. Lundgren, 1970: Light scattering and suspended particles in the eastern equatorial Pacific Ocean, *J. Geophys. Res.*, **75**, 2837–2845.

Behrenfeld M. J., and P. G. Falkowski, 1997: Photosynthetic rates derived from satellite-cased chlorophyll concentration, *Limnol. Oceanogr.*, **42**, 1–20.

Berthon, J.-F., E. Shybanov, M. E.-G. Lee, and G. Zibordi, 2007: Measurements and modeling of the volume scattering function in the coastal northern placeAdriatic Sea, *Appl. Opt.*, **46**, 5189–5203.

Beutell, R. G., and A. W. Brewer, 1949: Instruments for the Measurement of the Visual Range, *J. Sci. Instrum.*, **26**, 357–359.

Bogucki, D. J., J. A. Domaradzki, D. Stramski, and J. R. Zaneveld, 1998: Comparison of near-forward light scattering on oceanic turbulence and particles, *Appl. Opt.*, **37**, 4669–4677.

Bohren, C. F., and D. R. Huffman, 1983: *Absorption and Scattering of Light by Small Particles*, John Wiley, New York.

Boss, E., and W. S. Pegau, 2001: Relationship of light scattering at an angle in the backward direction to the backscattering coefficient, *Appl. Opt.*, **40**, 5503–5507.

Boss, E., M. S. Twardowski, and S. Herring, 2001: Shape of the particulate beam spectrum and its inversion to obtain the shape of the particle size distribution, *Appl. Opt.*, **40**, 4885–4893.

Boss, E., W. S. Pegau, M. Lee, M. S. Twardowski, E. Shybanov, G. Korotaev, and F. Baratange, 2004a: The particulate backscattering ratio at LEO-15 and its use to study particle composition and distribution, *J. Geophys. Res.*, **109**, C0101410.1029/2002JC001514.

Boss, E., D. Stramski, T. Bergmann, W. S. Pegau, and M. Lewis, 2004 b: Why should we measure the optical backscattering coefficient?, *Oceanography*, **17**, 44–49.

Boss, E., R. Collier, G. Larson, K. Fennel, and W. S. Pegau, 2007: Measurements of spectral optical properties and their relation to biogeochemical variables and processes in Crater Lake, Crater Lake National Park, OR, *Hydrobiologia*, **574**, 149–159.

Briggs, N., M. J. Perry, I. Cetinic, C. Lee, E. D'Asaro, A. Gray, and E. Rehm, 2011: Underwater gliders observe an aggregate 1 flux event in high vertical and temporal resolution during the North Atlantic spring bloom, *Deep Sea Res. I*, **58**, 1031–1039.

Chami, M., E. B. Shybanov, T. Y. Churilova, G. A. Khomenko, M. Lee, O. V. Martynov, G. A. Berseneva and G. K. Korotaev, 2005: Optical properties of the particles in the Crimea coastal waters (Black Sea), *J. Geophys. Res.*, **110**, C11020, doi:10.1029/2005JC003008.

Chami, M., E. Marken, J. J. Stamnes, G. Khomenko, and G. Korotaev, 2006: Variability of the relationship between the particulate backscattering coefficient and the volume scattering function measured at fixed angles, *J. Geophys. Res.*, **111**, C05013.

Churnside, J. H., and P. L. Donaghay, 2009: Thin scattering layers observed by airborne lidar, *ICES J. Mar. Sci.*, **66**, 778–789.

Churnside, J. H., V. V. Tatarskii, and J. J. Wilson, 1998: Oceanographic lidar attenuation coefficients and signal fluctuations measured from a ship in the Southern California Bight, *Appl. Opt.*, **37**, 3105–3112.

Dall'Olmo, G., T. K. Westberry, M. J. Behrenfeld, E. Boss, and W. H. Slade, 2009: Significant contribution of large particles to optical backscattering in the open ocean, *Biogeosciences*, **6**, 947–967.

Dana, D. R., and R. A. Maffione, 2002: Determining the backward scattering coefficienti with fixed-angle backscattering sensors – Revisited, *Ocean Optics XVI*, CityplaceSanta Fe, StateNM.

Fournier, G. R., and J. L. Forand, 1994: Analytic phase function for ocean water. *Proc. SPIE*, **2258**, 194–201.

Gordon, H. R., 1989: Dependence of the diffuse reflectance of natural waters on the sun angle, *Limnol. Oceangr.*, **34**(8), 1484–1489.

Gordon, H. R., 1993: Sensitivity of radiative transfer to small-angle scattering in the ocean: Quantitative assessment, *Appl. Opt.*, **32**, 7505–7511.

Gordon, H. R., O.B. Brown, and M. M. Jacobs, 1975: Computed relationships between the inherent and apparent optical properties, *Appl. Opt.*, **14**, 417– 427.

Gordon, H. R., M. R. Lewis, S. D. McLean, M. S. Twardowski, S. A. Freeman, K. J. Voss, and G. C. Boynton, 2009: Spectra of particulate backscattering in natural waters, *Opt. Express*, **17**, 16192–16208.

Guenther, G. C., 1985: Airborne laser hydrography: system design and performance factors, United States National Ocean Service, Office of Charting and Geodetic Services. National Technical Information Service, Rockville, MD. Springfield, VA.

Haubrich, J. M., Musser, J., and E. S. Fry, 2011: Instrumentation to measure the backscattering coefficient b_b for arbitrary phase functions, *Appl. Opt.*, **50**(21), 4134–4147.

Hewlett Packard, 1995: Application Brief I-012, Temperature compensation circuit for constant LED intensity, 2 pp.

Jackson, C ., L. M. Nilsson, and P. J. Wyatt, 1989: Characterization of biopolymers using a multi-angle light scattering detector with size-exclusion chromatography, *J. Appl. Polym. Sci., Appl. Polym. Symp.*, **43**, 99–114.

Jerlov, N. G., 1961: Optical measurements in the eastern North Atlantic. *Medd. Oceanogr. Inst. Göteborg, Ser. B*, 8.

Jerlov, N. G., 1968: *Optical Oceanography*. Elsevier, New York.

Jerlov, N. G., 1976: *Marine Optics*. Elsevier, New York.

Jonasz, M., and G. R. Fournier, 2007: *Light Scattering by Particles in Water: Theoretical and Experimental Foundations*, Academic Press.

Kopelevich, O. V., and V. I. Burenkov, 1971: The nephelometric method for determining the total scattering coefficienti of light in sea water, *Izv. Atmos. Oceanic Phys.*, **7**, 1280–1289.

Kullenberg, G., 1968: Scattering of light by Sargasso seawater. *Deep Sea Res.*, **15**, 423–432.

Kullenberg, G., 1972: A comparison between observed and computed light scattering functions, 2, *Rep. 19*, University of Copenhagen, Copenhagen.

Lee, M. E., and M. R. Lewis, 2003: A new method for the measurement of the optical volume scattering function in the upper ocean, *J. Atmos. Ocean. Technol.*, **20**, 563–571.

Loisel, H., X. Meriaux, J.-F. Berthon, and A. Poteau, 2007: Investigation of the optical backscattering to scattering ratio of marine particles in relation to their biogeochemical composition in the eastern English Channel and southern North Sea, *Limnol. Oceanogr.*, **52**(2), 739–752.

Ma, X., J. Q. Lu, R. S. Brock, K. M. Jacobs, P. Yang, and X. Hu, 2003: Determination of complex refractive index of polystyrene microspheres from 370 to 1610 nm, *Phys. Med. Biol.*, **48**, 4165–4172.

Maffione, R. A., and D. R. Dana, 1997: Instruments and methods for measuring the backward scattering coefficienti of ocean waters, *Appl. Opt.*, **36**, 6057–6067.

Matheson, L. A., and J. L. Saunderson, 1952: *Optical and Electrical Properties of Polystyrene, Styrene: Its Polymers, Copolymers and Derivatives*, R. H. Boundy and R. F. Boyer, eds., Reinhold Publishing Corporation, New York, pp. 517–546.

McKee, D., M. Chami, I. Brown, V. Sanjuan Calzado, D. Doxaran, and A. Cunningham, 2009: Role of measurement uncertainties in observed variability in the spectral backscattering ratio: a case study in mineral-rich coastal waters, *Appl. Opt.*, **48**, 4663–4675.

Mikkelsen, O.A., T. G. Milligan, P. S. Hill, R. J. Chant, C. F. Jago, S. E. Jones, V. Krivtsov, and G. Mitchelson-Jacob, 2008: The influence of schlieren on in situ optical measurements used for particle characterization, *Limnol. Oceanogr.: Methods*, **6**, 133–143.

Mishchenko, M. I., J. W. Hovenier, and L. D. Travis, 2000: *Light Scattering by Nonspherical Particles*, Academic Press, San Diego, CA.

Mobley, C. D., 1994: *Light and Water: Radiative Transfer in Natural Waters*, Academic Press, San Diego, CA.

Mobley, C. D., L. K. Sundman, and E. Boss, 2002: Phase function effects on oceanic light fields, *Appl. Opt.*, **41**, 1035–1050.

Moore, C., M. S. Twardowski, and J. R. V. Zaneveld, 2000: The ECO VSF: a multiangle scattering sensor for determination of the volume scattering function in the backward direction, *Ocean Optics XV*, Monaco, 16–20 October.

Morel, A., 1966: Etude expérimentale de la diffusion de la lumière par l'eau, le solutions de chlorine de sodium et l'eau de mer optiquement pure. *J. de Chimie Physique*, **10**, 1359–1366.

Morel, A., 1973: Diffusion de la lumiere par les eaux de mer. Resultats experimentaux et approche theorique, in *Optics of the Sea*, AGARD Lecture Series, No. 61, NATO, pp. 3.1.1–3.1.76.

Morel, A., 1974: Optical properties of pure water and pure seawater, in *Optical Aspects of Oceanography*, N. G. Jerlov and E. Steeman, eds. (Academic Press, London), pp. 1–24.

Morel, A., and B. Gentili, 1983: Diffuse reflectance of oceanic waters. II. Bidirectional aspects, *Appl. Opt.*, **32**, 6864–6879.

Morel, A., K. Voss, and B. Gentilli, 1995: Bidirectional reflectance of oceanic waters: A comparison of modeled and measured upward radiance fields, *J. Geophys. Res.*, **100**, 13,143–13,150.

Neukermans, G., H. Loisel, X. Mériaux, R. Astoreca, and D. McKee, 2012: In situ variability of mass-specific beam attenuation and backscattering of marine particles with respect to particle size, density, and composition, *Limnol. Oceanogr.*, **57**(1), 124–144.

Nikolov, I. D., and C. D. Ivanov, 2000: Optical plastic refractive measurements in the visible and the near-infrared regions, *Appl. Opt.*, **39**, 2067–2070.

Oishi, T., 1990: Significant relationship between the backward scattering coefficienti of sea water and the scatterance at 120°, *Appl. Opt.*, **29**, 4658–4665.

Petzold, T. J., 1972: Volume scattering functions for selected ocean waters, Tech. Rep., Scripps Institution of Oceanography, 72–78.

Prentice, J. E., A. D. Weidemann, W. S. Pegau, K. J. Voss, M. E. Lee, E. Shybanov, O. Martynov, A.E. Laux, A. Briggs, and G. Chang, 2002: Laboratory comparisons of optical scattering instrumentation, *Ocean Optics XVI*, Santa Fe, New Mexico.

Quinby-Hunt, M. S., A. J. Hunt, K. Lofftus, and D. Shapiro, 1989: Polarized-light scattering studies of marine chlorella, *Limnol. Oceanogr.*, **34**, 1587–1600.

Reynolds, K. J., J. P. De Kock, L. Tarassenko and J. T. B. Moyle, 1991: Temperature dependence of LED and its theoretical effect on pulse oximetry, *Br. J. Anaesth.*, **67**(5), 638–643.

Stramska, M., and D. Stramski, 2005: Variability of particulate organic carbon concentration in the north polar Atlantic based on ocean color observations with Sea-viewing Wide Field-of-view Sensor (SeaWiFS), *J. Geophys. Res.*, **110**, C10018, doi:10.1029/2004JC002762.

Stramski, D., and D. A. Kiefer, 1991: Light scattering by microorganisms in the open ocean, *Prog. Oceanogr.*, **28**, 343–383.

Stramski, D., R. A. Reynolds, M. Kahru, and B. G. Mitchell, 1999: Estimation of particulate organic carbon in the ocean from satellite remote sensing, *Science*, **5425**, 239–241.

Stramski, D., E. Boss, D. Bogucki, and K. J. Voss, 2004: The role of seawater constituents in light backscattering in the ocean, *Progr. Oceanogr.*, **61**(1), 27–56.

Stramski, D., R. A. Reynolds, M. Babin, S. Kaczmarek, M. R. Lewis, R. Röttgers, A. Sciandra, M. Stramska, M. S. Twardowski, and H. Claustre, 2008: Relationships between the surface concentration of particulate organic carbon and optical properties in the eastern South Pacific and eastern Atlantic Oceans, *Biogeosciences*, **5**, 171–183.

Sullivan, J. M., and M. S. Twardowski, 2009: Angular shape of the oceanic particulate volume scattering function in the backward direction, *Appl. Opt.*, **48**(35), 6811–6819.

Sullivan, J. M., M. S. Twardowski, P.L. Donaghay, and S. Freeman, 2005: Using optical scattering to discriminate particle types in coastal waters, *Appl. Opt.*, **44**, 1667–1680.

Sullivan, J. M., P. L. Donaghay, and J. E. B. Rines, 2010: Coastal thin layer dynamics: consequences to biology and optics, *Cont. Shelf Res.*, **30**(1): 50–65. doi:10.1016/j.csr.2009.07.009.

Sun, D. Y. Li, Q. Wang, J. Gao, H. Lv, C. Le, and C. Huang, 2009: Light scattering properties and their relation to the biogeochemical composition of turbid productive waters: a case study of Lake Taihu, *Appl. Opt.*, **48**, 1979–1989.

Twardowski, M. S., E. Boss, J. B. Macdonald, W. S. Pegau, A. H. Barnard, and J. R. V. Zaneveld, 2001: A model for estimating bulk refractive index from the optical backscattering ratio and the implications for understanding particle composition in case I and case II waters, *J. Geophys. Res.*, **106**(C7), 14129–14142.

Twardowski, M. S., M. R. Lewis, A. H. Barnard, and J. R. V. Zaneveld, 2005: Water instrumentation and platforms for ocean color remote sensing applications, in *Remote Sensing and Digital Image Processing, 1*, Vol. 7: Remote Sensing of Coastal Aquatic Environments, pp. 69–100.

Twardowski, M. S. H. Claustre, S. A. Freeman, D. Stramski, and Y. Huot, 2007: Optical backscattering properties of the 'clearest' natural waters, *Biogeosciences*, **4**, 1041–1058.

Twardowski, M. S., X. Zhang, S. Vagle, J. Sullivan, S. Freeman, H. Czerski, Y. You, L. Bi, and G. Kattawar, 2012: The optical volume scattering function in a surf zone inverted to derivesediment and bubble particle subpopulations, *J. Geophys. Res.*, **117**, doi:10.1029/2011JC007347.

Tyler, J. E. and W. H. Richardson, 1958: Nephelometer for the measurement of volume scattering function in situ, *J. Opt. Soc. Am.*, **48**, 354–357.

Tzortziou, M., J. R. Herman, C. L. Gallegos, P. J. Neale, A. Subramaniam, L. W. Harding, Jr., and Z. Ahmad. 2006: Bio-optics of the Chesapeake Bay from measurements and radiative transfer closure. *Est. Coast. Shelf Sci.*, **68**, 348–362.

Ulloa, O., S. Sathyendranath, and T. Platt. 1994: Effect of the particle-size distribution on the backscattering ratio in seawater, *Appl. Opt.*, **30**, 7070–7077.

Vaillancourt, R. D., C. W. Brown, R. R. L. Guillard, and W. M. Balch, 2004: Light backscattering properties of marine phytoplankton: relationships to cell size, chemical composition, and taxonomy, *J. Plankton Res.*, **26**, 191–212.

Volten, H., J. F. de Haan, J. W. Hovenier, R. Schreurs, and W. Vassen, 1998: Laboratory measurements of angular distributions of light scattered by phytoplankton and silt, *Limnol. Oceangr.*, **43**, 1180–1197.

Voss, K., and A. Morel, 2005: Bidirectional reflectance function for oceanic waters with varying chlorophyll concentrations: Measurements versus predictions. *Limnol. Oceanogr.*, **50**(2), 698–705.

Voss, K. J., A. Chapin, M. Monti, and H. Zhang, 2000: Instrument to measure the bidirectional reflectance distribution function of surfaces, *Appl. Opt.*, **39**, 6197–6206.

Whitmire, A. L., E. Boss, T. J. Cowles, and W. S. Pegau, 2007: Spectral variability of the particulate backscattering ratio, *Opt. Express*, **15**, 7019–7031.

Whitmire, A. L., W. S. Pegau, L. Karp-Boss, E. Boss, and T. J. Cowles, 2010: Spectral backscattering properties of marine phytoplankton cultures, *Opt. Express*, **18**, 15073–15093.

Zaneveld, J. R. V., 1995: A theoretical derivation of the dependence of the remotely sensed reflectance on the inherent optical properties, *J.Geophys Res.*, **100**(C7), 13, 135–13, 142.

Zaneveld, J. R. V., and J. C. Kitchen, 1995: The variation in the inherent optical properties of phytoplankton near an absorption peak as determined by various models of cell structure, *J. Geophys. Res.*, **100**, 13, 309–13, 320.

Zhang, X., and L. Hu, 2009: Scattering by pure seawater at high salinity, *Opt. Express*, **17**(15), 12685–12691.

Zhang, X., L. Hu, and M.-X. He, 2009: Scattering by pure seawater: effect of salinity, *Opt. Express*, **17**, 5698–5710.

Zhang, X., M. S. Twardowski, and M. Lewis, 2011: Retrieving composition and sizes of oceanic particle subpopulations from the volume scattering function, *Appl. Opt.*, **50**, 1240–1259.